

**EARTHQUAKE DAMAGE DETECTION USING WATERSHED  
SEGMENTATION AND INTENSITY-GRADIENT ORIENTATION  
APPROACHES**

**A THESIS SUBMITTED TO  
THE GRADUATE SCHOOL OF NATURAL AND APPLIED SCIENCES  
OF  
MIDDLE EAST TECHNICAL UNIVERSITY**

**BY**

**EMRE SÜMER**

**IN PARTIAL FULFILLMENT OF THE REQUIREMENTS  
FOR  
THE DEGREE OF MASTER OF SCIENCE  
IN  
GEODETIC AND GEOGRAPHICAL INFORMATION TECHNOLOGIES**

**SEPTEMBER 2004**

Approval of the Graduate School of Natural and Applied Sciences

---

Prof. Dr. Canan ÖZGEN  
Director

I certify that this thesis satisfies all the requirements as a thesis for the degree of Master of Science.

---

Assoc. Prof. Dr. Oğuz IŞIK  
Head of Department

This is to certify that i have read this thesis and that in my opinion it is fully adequate, in scope and quality, as a thesis for the degree of Master of Science.

---

Assist. Prof. Dr. Mustafa TÜRKER  
Supervisor

Examining Committee Members

Prof. Dr. Vedat TOPRAK	(METU,GGIT)	_____
Assist. Prof. Dr. Mustafa TÜRKER	(METU,GGIT)	_____
Prof. Dr. Hayri SEVER	(Başkent Univ.)	_____
Assoc. Prof. Dr. K. Önder ÇETİN	(METU,CE)	_____
Assist. Prof. Dr. Bahattin COŞKUN	(METU,CE)	_____

**I hereby declare that all information in this document has been obtained and presented in accordance with academic rules and ethical conduct. I also declare that, as required by these rules and conduct, I have fully cited and referenced all material and results that are not original to this work.**

Name, Last name: Emre SÜMER

Signature:

## **ABSTRACT**

### **EARTHQUAKE DAMAGE DETECTION USING WATERSHED SEGMENTATION AND INTENSITY-GRADIENT ORIENTATION APPROACHES**

Sümer, Emre

M.S., Department of Geodetic and Geographic Information Technologies

Supervisor: Assist. Prof. Dr. Mustafa TÜRKER

September 2004, 100 pages

Earthquake is one of the most destructive natural disasters on earth. Rapid and reliable post-quake damage assessment has an important role to reduce the drastic effects of an earthquake by setting the responsible agencies in motion. In this study, the collapsed buildings due to earthquake were detected from post-event aerial images. Two approaches were proposed to detect the collapsed buildings. These approaches were implemented in a selected urban area of Golcuk. The first approach was based on the analysis of shadow casting edges. First, the shadow casting edges of the buildings were identified and a buffer zone was generated for each building polygon along these edges. Then, the shadow regions were detected using the watershed segmentation algorithm. This was followed by measuring the agreement between the shadow producing edges of the buildings and their corresponding shadows. Of the 284 buildings analyzed, 229 were successfully labeled as collapsed or un-collapsed providing an overall accuracy of 80,63%.

In the second approach, a two-branch method based on building light intensities and the gradient orientation was used. In the first branch, an intensity threshold was determined and applied to building image patches. Then, a pixel ratio was computed to categorize the buildings. In the second branch, a series of processings were carried out including the smoothing of the building image patches and the determination of the magnitude and the orientation of the gradient. Then, an optimum angle threshold was determined to label the buildings. The final decision about the condition of a building was made by integrating the two branches. Of the 284 buildings analyzed, 254 were correctly labeled providing an overall accuracy of 89,44%. The same assessments were repeated after generating a one-pixel wide buffer zone around the building polygons and an overall accuracy of 90,85% was obtained.

The results of the proposed approaches prove that the collapsed buildings caused by the earthquake can be successfully detected from post-event aerial images.

Keywords: Image Processing, Earthquakes, Detection, Aerial, Building.

## ÖZ

### WATERSHED KESİMLEMESİ VE YOĞUNLUK-EĞİM YÖNELİMİ YAKLAŞIMLARI KULLANILARAK DEPREM HASAR TESPİTİ

Sümer, Emre

Yüksek Lisans, Jeodezi ve Coğrafi Bilgi Teknolojileri E.A.B.D  
Tez Yöneticisi: Yrd. Doç. Dr. Mustafa TÜRKER

Eylül 2004, 100 sayfa

Deprem, yerküredeki en yıkıcı doğal felaketlerden birisidir. Hızlı ve güvenilir bir deprem sonrası hasar değerlendirmesi, depremin şiddetli etkilerini ilgili kuruluşları devreye sokarak azaltmada önemli bir role sahiptir. Bu çalışmada, deprem nedeniyle yıkılmış binalar, deprem sonrası hava fotoğraflarından tespit edilmiştir.

Yıkılmış binaların tespitinde iki yaklaşım önerilmiştir. Bu yaklaşımlar, Gölcük'ten seçilen kentsel bir bölge üzerinde uygulanmıştır. İlk yaklaşım, gölge oluşturan kenarların analizi temeline dayanmaktadır. İlk önce, binaların gölge üreten kenarları saptanmış ve her bir bina çokgeni için bu kenarlar boyunca bir tampon alan oluşturulmuştur. Daha sonra, gölge alanları watershed kesimleme algoritması kullanılarak tespit edilmiştir. Bunu, binaların gölge üreten kenarlarıyla ilgili gölgesinin arasındaki uyuşmanın ölçülmesi takip etmiştir. Analiz edilen 284 bina içinden 229 tanesi %80,63'lük bir genel doğruluk sağlayarak başarılı bir biçimde "yıkılmış" veya "yıkılmamış" olarak tanımlanmıştır.

İkinci yaklaşımda ise, bina ışık yoğunluğu ve eğim yönünü temel alan iki bölümlü bir yöntem kullanılmıştır. Birinci bölümde, bir yoğunluk eşik değeri belirlenmiş ve bina görüntülerine uygulanmıştır. Daha sonra, binaların kategorize edilmeleri için bir piksel oranı belirlenmiştir. İkinci bölümde ise, bina görüntülerinin yumuşatılması ve eğim büyüklüğünün ve yönünün belirlenmesini içeren bir grup işlemler yerine getirilmiştir. Sonrasında, binaların sınıflandırılması için en uygun açı eşik değeri belirlenmiştir. İki bölümün birleştirilmesiyle, bir binanın durumu hakkında son bir karara varılmıştır. Analiz edilen 284 bina içinden 254 tanesi %89,44'lük bir genel doğruluk sağlayarak başarılı bir şekilde sınıflandırılmıştır. Benzer değerlendirmeler, bina çokgenleri etrafında tek piksellik bir tampon alan oluşturulduktan sonra tekrarlanmış ve %90,85'lik bir genel doğruluk elde edilmiştir.

Önerilen yaklaşımların sonuçları göstermektedir ki deprem nedeniyle yıkılmış binalar, deprem sonrası hava fotoğraflarından başarıyla tespit edilebilmektedir.

Anahtar Kelimeler: Görüntü İşleme, depremler, tespit, havaya ilişkin, bina.

To My Wife

## **ACKNOWLEDGMENTS**

I wish to express my deepest gratitude to my supervisor, Assist. Prof. Dr. Mustafa TÜRKER, for his guidance, advice, criticism and encouragement and insight throughout my research.

I would also thank to Assoc. Prof. Dr. Volkan ATALAY for his support and assistance.

I would like to thank my dean, Prof. Dr. İmdat KARA, and my chairman, Prof. Dr. Hayri SEVER, from Baskent University for their insight and patience throughout my study.

I would like to express my sincere gratitude to Ali Özgün OK, Hasan OĞUL and Nurcan DURAK for their suggestions, assistance and encouragement throughout my thesis.

Finally, I cordially would like to thank my wife and parent for their affection, support and patience during my masters program.

## TABLE OF CONTENTS

ABSTRACT.....	iv
ÖZ.....	vi
ACKNOWLEDGEMENTS.....	ix
TABLE OF CONTENTS.....	x
LIST OF TABLES.....	xiii
LIST OF FIGURES.....	xv
CHAPTER	
1. INTRODUCTION.....	1
1.1 Study Area and Data Description.....	2
1.2 Organization of the Thesis.....	5
2. PAST STUDIES FOR DAMAGE DETECTION FROM AERIAL AND SPACE IMAGES.....	7
2.1 The Remote Sensing Technology in Earthquake Studies.....	7
2.2 Past Studies Related to Damage Detection.....	8
3. BUILDING DAMAGE DETECTION USING WATERSHED SEGMENTATION.....	15
3.1 The Methodology.....	15
3.2 Building Selection.....	17
3.3 Shadow Edge Detection.....	19
3.4 Buffer Zone Generation .....	21
3.5 Watershed Segmentation.....	21
3.6 Building Condition Assessment.....	24
3.7 The Results.....	25

4.	BUILDING DAMAGE DETECTION USING BUILDING INTENSITY-GRADIENT ORIENTATION APPROACH.....	31
4.1	The Methodology.....	31
4.2	Building Selection.....	33
4.3	The Building Intensity Approach.....	34
4.4	The Gradient Orientation Approach.....	37
4.4.1	Image Pre-processing.....	38
4.4.2	The Calculation of the Gradient Orientation.....	39
4.4.3	Threshold Determination for the Optimum Standard Deviation.....	41
4.5	Assessments of the Conditions of the Buildings by Integrating Both Approaches.....	43
4.6	The Results.....	45
5.	DEVELOPING A BUILDING DAMAGE DETECTION SOFTWARE.....	50
5.1	System Design.....	50
5.2	Watershed Segmentation Component.....	53
5.3	Building Intensity – Gradient Orientation Component.....	56
5.4	Image Analysis Component.....	59
6.	DISCUSSIONS OF THE RESULTS.....	62
6.1	Comparison of the Two Approaches.....	62
6.2	Discussions.....	65
7.	CONCLUSIONS AND RECOMMENDATIONS.....	72
7.1	Conclusions of Watershed Segmentation Approach.....	72
7.2	Conclusions of Building Intensity-Gradient Orientation Approach.....	73
7.3	Recommendations.....	74
	REFERENCES.....	76
	APPENDICES	
	A. ERROR MATRICES FOR THE VARYING THRESHOLD VALUES BETWEEN 20% AND 80%.....	80

B. CALCULATIONS OF THE ACCURACY INDICES FOR THE THRESHOLD LEVELS BETWEEN 20% AND 80%.....	82
C. CALCULATION OF OPTIMUM BUILDING INTENSITY THRESHOLD LEVEL.....	88
D. CALCULATION OF OPTIMUM BUILDING INTENSITY THRESHOLD LEVEL WITH 1 PIXEL WIDE BUFFER REGION.....	90
E. SOURCE CODE OF THE WATERSHED SEGMENTATION COMPONENT.....	92
F. SOURCE CODE OF THE BUILDING INTENSITY-GRADIENT ORIENTATION COMPONENT.....	95
G. THE DISTRIBUTION OF THE COLLAPSED, UN-COLLAPSED AND INCORRECTLY DETECTED BUILDINGS FOR THE WATERSHED SEGMENTATION APROACH.....	98
H. THE DISTRIBUTION OF THE COLLAPSED, UN-COLLAPSED AND INCORRECTLY DETECTED BUILDINGS FOR THE BUILDING INTENSITY – GRADIENT ORIENTATION APROACH.....	99
I. THE DISTRIBUTION OF THE COLLAPSED, UN-COLLAPSED AND INCORRECTLY DETECTED BUILDINGS FOR THE BUILDING INTENSITY – GRADIENT ORIENTATION APROACH WITH A ONE-PIXEL WIDE BUFFER.....	100

## LIST OF TABLES

### TABLES

3.1.	The calculation of (building / shadow) pixel ratios for building # 175.....	25
3.2.	The accuracy indices for the threshold values between 20% and 80%.....	27
3.3.	The error matrix for the threshold value of 50%.....	27
3.4.	The error matrix for the optimum threshold value of 50% with accuracies.....	30
4.1.	The accuracy indices for the pixel ratios between 10% and 90%.....	45
4.2.	The accuracy indices for the pixel ratios between 10% and 90% in the buffered case.....	46
4.3.	The error matrix for the optimum pixel ratio and standard deviation threshold levels in the un-buffered case.....	48
4.4.	The error matrix for the optimum pixel ratio and standard deviation threshold levels in the buffered case.....	48
6.1.	The comparison of the proposed approaches in terms of overall accuracies.....	62
6.2.	The comparison of the user's and producer's accuracies for collapsed and un-collapsed buildings.....	63
6.3.	The comparison of the correctly and incorrectly detected buildings with omission and commission errors.....	64
6.4.	The distribution of the mis-detected buildings according to six cases.....	70
A.1.	Error matrix for the threshold level of 20%.....	80
A.2.	Error matrix for the threshold level of 30%.....	80
A.3.	Error matrix for the threshold level of 40%.....	80
A.4.	Error matrix for the threshold level of 50%.....	80

A.5.	Error matrix for the threshold level of 60%.....	81
A.6.	Error matrix for the threshold level of 70%.....	81
A.7.	Error matrix for the threshold level of 80%.....	81

## LIST OF FIGURES

### FIGURES

1.1.	Location of the study area.....	3
1.2.	Distribution of the surface areas of the buildings.....	4
2.1.	Flow of the proposed method by Yanamura and Saji, (2003).....	10
2.2.	The block diagram of the damage assessment system architecture developed during RADATT project by Gamba and Casciati (1998).....	12
3.1.	Damage detection using watershed segmentation.....	16
3.2.	(a) Original aerial photo, (b) histogram-equalized aerial photo, (c) histogram of the original aerial photo, (d) histogram of the histogram-equalized photo.....	17
3.3.	(a) The edges of building # 175 and (b) the structure of vector data.....	18
3.4.	Minimum bounding rectangle and the buffer bound generated on building # 175.....	19
3.5.	(a) The Euclidean distances ( $d_1, d_2, d_3, d_4$ ) and the angle of illumination, (b) the shadow producing edges of building # 175.....	20
3.6.	Buffer zone generation along the shadow producing edges.....	21
3.7.	Watershed segmentation in one dimension: (a) gray-level profile of the image data; (b) watershed segmentation – local minima of gray-level (altitude) yield catchment basins; local minima define the watershed lines.....	22
3.8.	(a) The starting pixels (markers) for watershed transform, and (b) the segmented output after the watershed transform.....	23
3.9.	The shadow and building regions used in the assessment of the building condition.....	25
3.10.	The process of optimum threshold determination and accuracy	

assessment.....	26
3.11. The change of the overall accuracy as the threshold changes.....	29
4.1. Damage detection using building intensity – gradient orientation analysis.....	32
4.2. A building polygon (a) with no buffer area,(b) with a one-pixel buffer area.....	34
4.3. (a) An un-collapsed building with low intensity and (b) a collapsed building with higher intensity.....	35
4.4. The intensity histogram for (a) un-collapsed buildings and (b) collapsed buildings.....	36
4.5. A building image after applying the threshold value of 145.....	36
4.6. The intensity histograms for (a) un-collapsed buildings and (b) collapsed buildings that have one-pixel wide buffer bound.....	37
4.7. (a) A collapsed building with random gradient direction and (b) an un-collapsed building with regular gradient direction.....	38
4.8. A building image patch (a) before smoothing and (b) after smoothing.....	39
4.9. (a) The gradient magnitude and (b) the gradient orientation of a building patch.....	40
4.10. (a) An un-collapsed building and (b) a collapsed building with un-biased frequencies.....	41
4.11. (a) An un-collapsed building and (b) a collapsed building with un-biased frequencies after mapping the frequency values between 0 and 100.....	42
4.12. The change of the overall accuracy as the pixel ratio changes.....	47
4.13. The change of the overall accuracy as the pixel ratio changes in the buffered case.....	47
5.1. The architecture of the system.....	52
5.2. Main menu of the damage detection software.....	53
5.3. A general view of the watershed segmentation interface and the results of the manual segmentation.....	54
5.4. View of the automatic segmentation.....	55

5.5.	Main menu of the damage detection software with second option selected.....	56
5.6.	General view of the building intensity – gradient orientation interface and the result of the manual detection.....	57
5.7.	View of the automatic detection.....	58
5.8.	Main menu of the image enhancement.....	59
5.9.	(a) High brightness image, (b) low brightness image, (c) high contrast image, (d) low contrast image, (e) high gamma image, (f) low gamma image.....	60
5.10.	The histogram of the (a) original image and (b) equalized image.....	60
5.11.	Main menu of the edge detection.....	61
5.12.	Output images after applying (a) Prewitt, (b) Sobel, (c) Roberts, (d) Laplacian of Gaussian and (e) Canny edge filters.....	61
6.1.	An example for the limitation # 1.....	66
6.2.	An example for the limitation # 2.....	66
6.3.	An example for the limitation # 3.....	67
6.4.	An example for the limitation # 4.....	68
6.5.	An example for the limitation # 5.....	68
6.6.	An example for the limitation # 6.....	69
G.1.	The building distribution for the Watershed Segmentation Approach.....	98
H.1.	The building distribution for the Building Intensity – Gradient Orientation Approach.....	99
I.1.	The building distribution for the Building Intensity – Gradient Orientation Approach with a one-pixel wide buffer.....	100

## CHAPTER 1

### INTRODUCTION

Natural disasters are defined as rapid and destructive events, which seriously threaten life and property on earth (Alexander, 1993). Earthquakes are one of the most significant natural catastrophes that cannot be predicted and prevented. Turkey is one of the countries that considerably suffers from this catastrophic event. On August 17, 1999, the urban areas of Golcuk, Yalova, Izmit and Istanbul were significantly damaged by a strong earthquake. The epicenter of the earthquake was  $40.702N^{\circ}$ ,  $29.987E^{\circ}$ , near the city of Izmit, the magnitude was 7.4 and the depth was 17 km (EDM, 2000). As a social damage, according to the Government Crisis Center, around 15.000 people died, 24.000 were injured and up to 600.000 people were forced to leave their homes. As a structural damage, about 41.000 structures including the residential and commercial buildings, and the public facilities were heavily damaged (Erdik, 2003).

The prevention of earthquakes is nearly impossible with today's technology and knowledge but according to Montoya (2002), with effective disaster management strategies such as preparedness, mitigation, response and recovery activities, the impact of the disasters can be avoided or reduced. For instance, the extent of the damage caused by a catastrophic event can be efficiently assessed using remote sensing technology that aims to set the corresponding agencies in motion to reduce the life losses.

Change detection is a widely used technique in remote sensing to detect the earthquake-induced changes. Image rationing and image differencing are the frequently used methods in change detection applied in post-earthquake

damage assessment studies. There are also several other techniques such as digital image classification and texture analysis to detect the damage caused by an earthquake. Besides, various kinds of data sources are available to be used in the post-earthquake damage assessment studies, which are nighttime imagery, optical imagery, radar imagery, aerial photography, aerial video imagery and airborne MSS imagery.

The objective of this study is to detect the collapsed buildings from post-event aerial imagery based on building shadows, brightness and the orientation of the gradient. This was achieved by proposing two different approaches: (i) Watershed Segmentation and (i) Building Intensity - Gradient Orientation. These approaches were implemented in a selected urban area of the city of Golcuk, which is one of the urban areas most strongly affected by the earthquake.

During this study, all the implementations and the processes were carried out using MATLAB® 6.5, which is a high-performance language for technical computing. Using this language, a program was developed that achieves the automated detection of the collapsed buildings using the two approaches. The data used in the detection process is fed into the program and the results of the analyses are obtained in both graphical and textual modes. The program also performs some additional operations, such as image enhancement and edge detection on the image of the study area.

### **1.1. Study Area and Data Description**

A selected urban area of the city of Golcuk was used as the study area. The area is located in Marmara region, which is located in the northwestern part of Turkey (Figure 1.1).

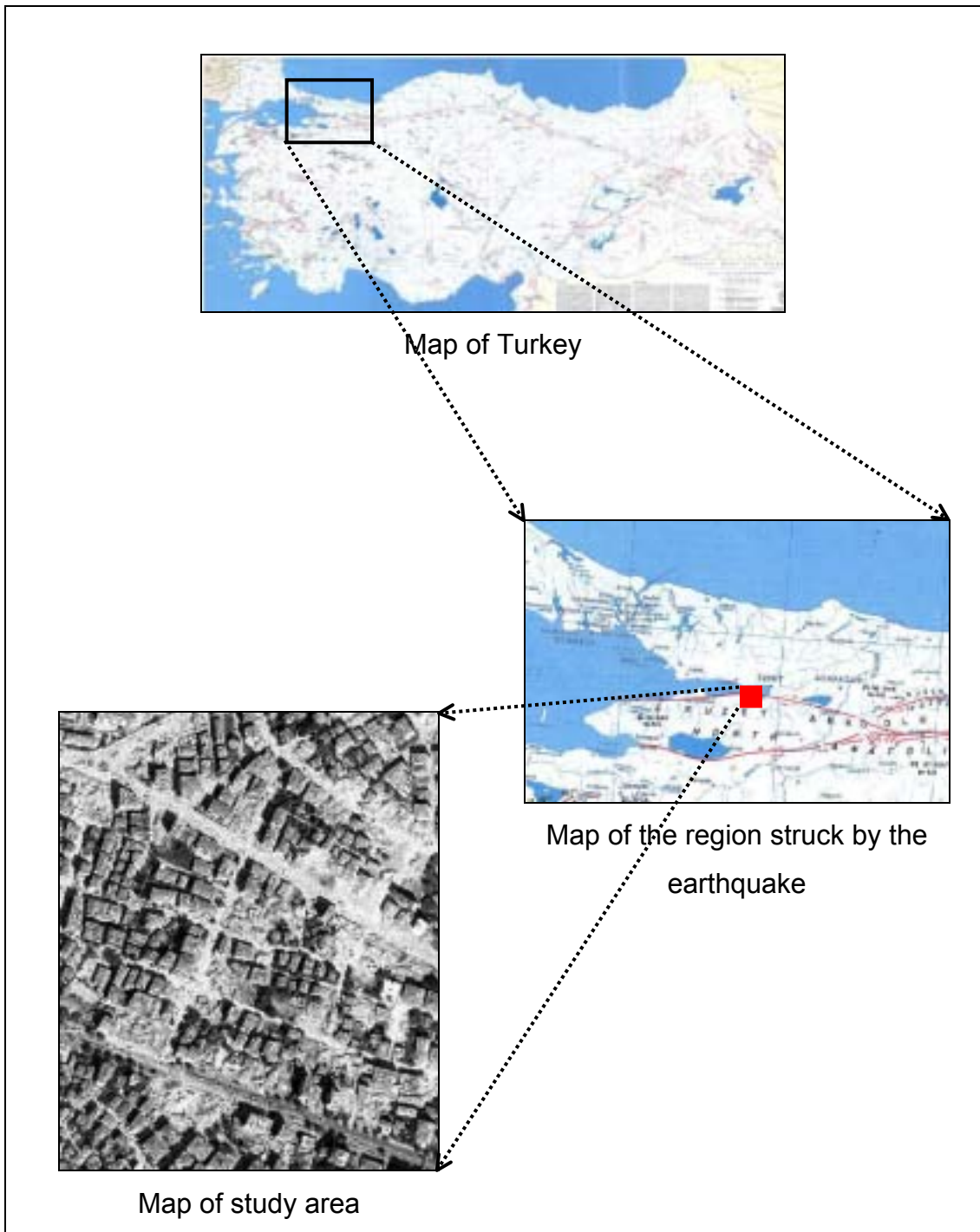


Figure 1.1. Location of the study area

The study area consists of 284 rectangular shaped buildings. It is known from a previous study (San, 2002) that 79 of the 284 buildings were collapsed and the remaining 205 buildings were un-collapsed. In the study area, the surface

area of the smallest building is 54 m<sup>2</sup> and the largest is 918 m<sup>2</sup>. The average surface area of all buildings is found to be 231 m<sup>2</sup>. The distribution of the surface areas of the buildings is illustrated in Figure 1.2.

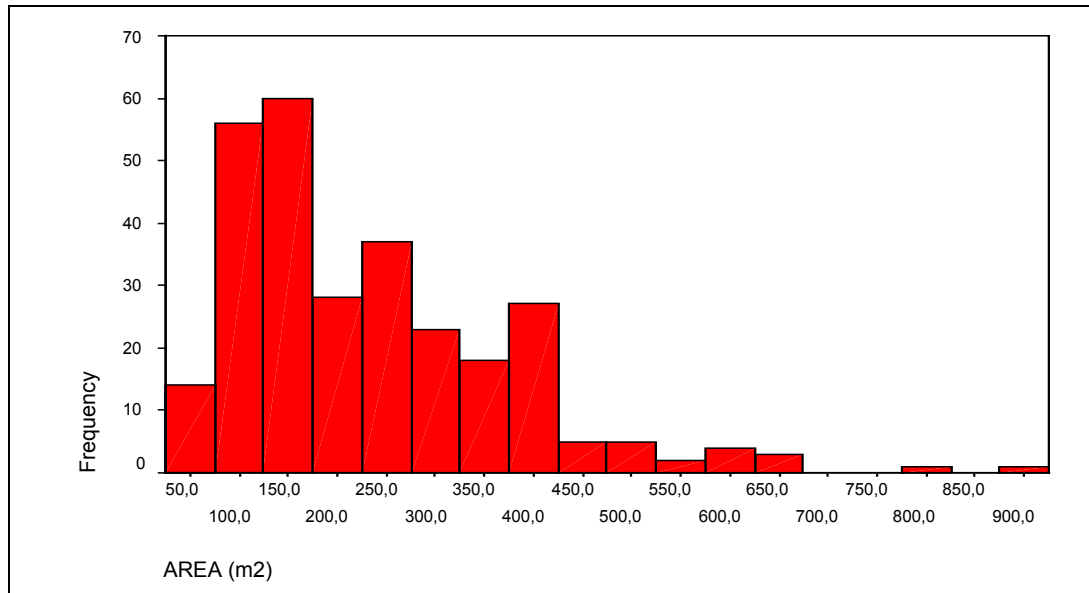


Figure 1.2. Distribution of the surface areas of the buildings

A post-earthquake panchromatic aerial photograph having 1-meter spatial resolution was used as the post-quake image data. The photographs covering the area were taken after the earthquake (in September 1999) at midday by the General Command of Mapping of Turkey. The scale of the aerial photo was 1/16,000 and it was scanned at 21 μm. The illumination direction and the sun angle determined by San (2002) were also available. The sun angle was computed as 135° from the post-event aerial photo. This means that the sun was in southeast of the aerial photo.

The vector building boundaries were also utilized in this study in order to assess the conditions of the buildings. This data set was also prepared by San (2002) by digitizing each building polygon. The vector data set contains, for each building, the Cartesian coordinates of the edge points.

## **1.2. Organization of the Thesis**

This thesis is composed of seven chapters. The next chapter (chapter 2) provides the literature review about the building damage assessment from aerial and space images, in terms of previous studies, data requirements and the methodology.

In chapter 3, the methodology that provides the detection of the collapsed buildings using the watershed segmentation algorithm is introduced. First, the methodology is summarized using a flowchart. Next, the building selection procedure and the utilization of the vector data are explained together with the aerial photo. Then, the determination of the shadow edges of each building is explained. This is followed by the buffer zone generation procedure. After that, the watershed segmentation step is explained and the results are presented. Finally, the accuracy assessment step is provided together with the final results.

The second methodology concerning the building intensity and the gradient orientation is described in chapter 4. First, the steps of the proposed method are presented. Then, the selection of the buildings is explained using the aerial photo and the vector building boundary information. Next, the details of the building intensity and the gradient orientation methods are discussed and the results are given. After that, the building assessment step that combines the results of the two methods is presented. At the end of the chapter, the accuracy assessment is carried out and then the final results are demonstrated.

The following chapter (chapter 5) presents the building damage detection software developed by the author. Introduction to software and the system architecture are given first. Then, the building damage detection components of the program are explained by means of inputs, outputs and other

processes. Lastly, the image analysis component is presented including image enhancement and edge detection options.

Chapter 6 contains the comparison of the proposed two approaches by means of accuracies and several statistics computed for the collapsed and un-collapsed buildings. Moreover, the reasons for incorrect detection of the buildings are discussed in this chapter by providing several examples.

The final chapter concludes the proposed methods and contains several recommendations arising from this study.

## **CHAPTER 2**

### **PAST STUDIES FOR DAMAGE DETECTION FROM AERIAL AND SPACE IMAGES**

This chapter includes the previous studies conducted on damage detection methods using air borne and space borne remote sensing technologies. First, the remote sensing technology in earthquake studies is introduced. Then, the past studies related to earthquake damage detection are presented by means of aerial or space images and applied methodologies.

#### **2.1. The Remote Sensing Technology in Earthquake Studies**

Remote sensing technology is an important tool to get useful information from earth surface features. Using this technology, it is possible to monitor the damages occurred by floods, droughts, fires, hurricanes, earthquakes and any other natural disasters. Remote sensing technology has been applied to many earthquakes occurred in different places and times on earth. Some examples of these are the Irpinia (Italy) earthquake in 1980, the Hyogoken-Nanbu (Kobe) earthquake in 1995, the Umbria (Italy) earthquake in 1997, the Chi-Chi (Taiwan) earthquake in 1999, the Quindio (Colombia) earthquake in 1999, the Kocaeli (Turkey) earthquake in 1999, the Gujarat earthquake (India) in 2001, the Bhuj earthquake (India) in 2001 and the El Salvador earthquake in 2001. These cases are examined in the next section in terms of data used and the methodology.

The earthquake damage assessment studies are examined according to the use of different data sources based on airborne and spaceborne imagery. Airborne remote sensing is one of the most important technologies for obtaining information about the regions struck by earthquakes. Observation of buildings and infrastructures in urban areas and collection of damage data are appropriate by using this technology. Aerial photographs and aerial video imagery are the major types of data used in airborne remote sensing technology (Yamazaki, 2001; Ozisik, 2004).

Spaceborne remote sensing is another important technology in monitoring earthquake-induced changes. The chief advantage of spaceborne remote sensing is the large area coverage compared with the airborne remote sensing. For this reason, it is usually used to gather information at regional scale. In damage assessment studies, spaceborne remote sensing can be used either in optical systems or in microwave systems. The data sources that mostly used with the spaceborne remote sensing technology are: nighttime imagery, optical imagery and the radar imagery.

## **2.2. Past Studies Related to Damage Detection**

In many applications of damage assessment and building detection, the aerial photography is widely used due to its advantages such as improved vantage point, permanent recording, broadened spectral sensitivity, the increased spatial resolution, and geometric fidelity. One of the frequently used applications of aerial photography is the detection of the buildings from their shadows. Irvin and McKeown (1989) state that the shadows are usually among the darkest areas in images and their extraction can be feasible using image processing techniques. They developed several methods to estimate the grouping of related structures together with the shape, verification and height of individual structures. In each method, the main approach used was the relation between structures and their cast shadows. Another study

concerning the building shadows was realized by Huertas and Nevatia (1988). They used building shadows to estimate the building heights. In addition, the shadows cast by the buildings were utilized in verification of the buildings. Their method was composed of four steps including line and corner detection, labeling of the corners based on shadows, tracing of object boundaries, and finally the verification of hypotheses.

Ishii *et al.* (2002) proposed a method, containing two cases, to detect the damaged areas after the Hyogoken-Nanbu earthquake from the aerial photographs of the Kobe city. In the first case, color and edge information were used to detect the damaged areas from a post-quake aerial photograph. Combining the color information with the edge information, the discrimination of the damaged areas from the non-damaged could be done successfully. In the second step, aerial photographs of the same area taken before and after the earthquake were available. They matched the two images by using the affine transform and also manually. Then, the colors of the corresponding pixels in each image were checked. Thus, the areas having color differences were examined. As a consequence, the two-case method was said to be fairly good in determining the damaged areas.

Aerial photos at varying scales were used in the study conducted by Van Westen and Hofstee (2001). Visual interpretation of the aerial photos belonging to the damaged area due to the 1999 Quindio, Colombia earthquake was performed. Four types of damage were detected including total collapse, roof collapse, partially damaged roof and no visible damage. The results of the visual interpretation were found to be satisfactory because of the good agreement with the results of the field survey.

In a different study, post earthquake airborne multi-spectral scanner images were used in assessing the damage caused by the Kobe earthquake in 1995 (Mitomi *et al.*, 2003). A classification-based method was developed. First, the training areas were selected using GIS data, based on field damage survey.

Then, the detection of the damaged and non-damaged buildings was performed using the maximum likelihood classification algorithm. The results were quite satisfactory and were in good agreement with the field survey data.

Yanamura and Saji (2003) developed a technique that provides the automatic detection of the damaged areas due to an earthquake from the aerial images taken before and after the event. The first step of the damage detection was registering the two aerial images by the help of a digital map. To do that, the perspective transformation was used. Then, the differences between the registered images were computed to detect the damaged areas. At the end, the damaged areas were detected correctly. The summary of their proposed method is illustrated in Figure 2.1.

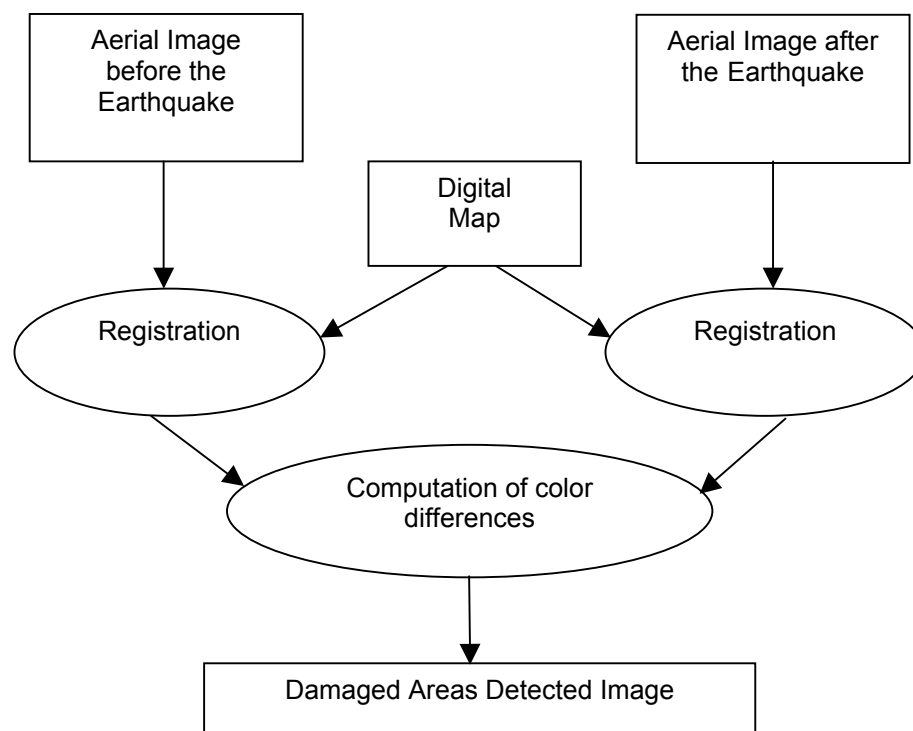


Figure 2.1. Flow of the proposed method by Yanamura and Saji (2003)

In a recent study, Turker and Cetinkaya (in press), detected the collapsed buildings caused by the 1999 Kocaeli, Turkey earthquake using digital elevation models (DEMs) created from the aerial photographs taken before (1994) and after (1999) the earthquake. The DEMs created from two epochs were differenced and the difference DEM was analyzed on a building-by-building basis for detecting the collapsed buildings. The producer's accuracy for collapsed buildings was computed to be 84%. Further, Turker and San (in press) utilized the cast shadows to detect the collapsed buildings due to Kocaeli, Turkey earthquake. The available vector building boundaries were used to match the shadow casting edges of the buildings with their corresponding shadows and to perform analysis in a building specific manner. Of the 80 collapsed buildings, 74 were detected correctly, providing 92.50% producer's accuracy.

Another kind of data source in airborne remote sensing is the aerial video imagery. In post-disaster damage detection, aerial video imagery taken from planes and helicopters are said to be quite practical and powerful due to its short response time and low cost (Ham, 1998; Yamazaki, 2001).

Images of the damaged buildings because of the 1995 Hyogoken-Nanbu (Kobe) earthquake were examined in order to provide the automatic detection of the damaged buildings (Hasegawa, 1999). The images were acquired by using aerial high-definition television (HDTV) data source. Using image processing techniques, the relationships between the degrees of building damage and the color information / edge intensity were investigated to detect the building damage. It was found that the results were in fairly good agreement with the ground surveys.

In a similar study, Mitomi *et al.* (2000) detected the damaged buildings by processing the aerial television images taken after the 1999 Kocaeli, Turkey and Chi-Chi, Taiwan earthquakes. The method was composed of defining the characteristics of the damage to wooden buildings based on hue, saturation,

brightness and the edge elements. First, the damaged pixels were extracted. Then, a threshold value for texture analysis was determined to estimate the distribution of damaged buildings. Once the results of the texture analysis were obtained, it was compared with the visual analysis. This approach was said to properly detect the collapsed buildings.

A near-real time earthquake damage assessment using the integration of GIS and remote sensing was performed by Gamba and Casciati (1998). Their approach comprised two phases. In the first phase, GIS was performed via collecting and analyzing data about buildings and infrastructures. In the second phase, the system receives near-real time imagery of the suffered area to perform change detection through shape analysis and perceptual grouping using the pre and post-event aerial images. The proposed system was initially applied to the Irpinia earthquake occurred in 1980 and then to the Umbria earthquake in 1997. The results were found to be quite satisfactory as the method was successful in determining almost all the buildings that were not destroyed even if a few errors were present. Figure 2.2 illustrates the diagram of the damage assessment system architecture developed by Gamba and Casciati (1998).

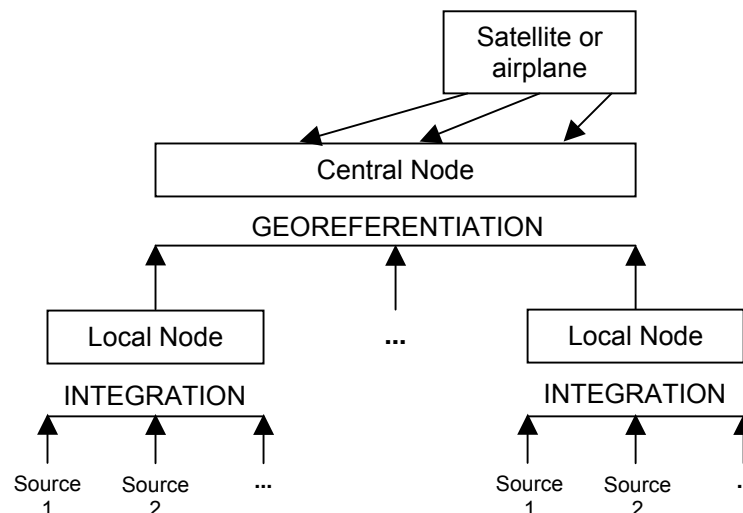


Figure 2.2. The block diagram of the damage assessment system architecture developed during the RADATT project by Gamba and Casciati (1998)

Huyck *et al.* (2003) used change detection algorithms to identify areas where complete collapse of buildings occurred for the Kocaeli earthquake of 1999. In this study, SPOT and SAR data were used as optical and radar data respectively. A series of algorithms were developed to show the differences between before and after event images. To validate these algorithms, the results of the analysis were compared with the ground truth data obtained by the Japanese investigation team. The comparison results proved that a good agreement was encountered between the two data sets.

Detection of damage for the January 13, 2001 El Salvador earthquake was conducted using Landsat-7 images by Estrada *et al.* (2001). Satellite images taken before and after the disaster were compared to identify the location of landslides and hard hit urban areas. It was performed by rationing between bands in visible portions together with the sharpening of the multi-spectral bands by merging with the panchromatic band. As a consequence of this study, the major landslides were successfully identified by manual inspection.

In a similar study, an earthquake damage detection method that compares the optical images with panchromatic bands of Landsat-7 was developed. (Yusuf *et al.* 2001). To do that, two different images of the disaster area due to the 2001 Gujarat, India earthquake acquired in January (before the earthquake) and in February 2001 (after the earthquake) were investigated. First, the differences in reflection intensity (digital number) of the two images were calculated and then, the estimated impacted area was abstracted on a pixel unit based on the obtained frequency distributions of the differences in the optical sensor values. After that, the significant changes in the reflectance were revealed. Finally, the accuracy of the results were assessed by a classification method and good correspondences were shown in the most of damaged distributions.

Chiroiu and Andre (2001) proposed a multidisciplinary approach based on high-resolution satellite data and earthquake engineering to assess the

damage caused by Bhuj, (India), Earthquake of January 26<sup>th</sup>, 2001. GIS was also used in order to display the spatial distribution of damages. The data used in this study was a 1-meter IKONOS multispectral simulation (a combination of 1 meter panchromatic and 4 meters multispectral) taken after the earthquake and a 2-meter panchromatic image obtained by KVR-1000 satellite before the earthquake. In automatic detection of damages, the high-resolution images taken before and after the earthquake were compared in terms of reflectance. At the same time, a radiometric improvement was applied to obtain a higher accuracy of the image, followed by a high-resolution filter and a false color composition was also made to illustrate the reflectance variation between the two scenes. The results were found to be moderately satisfactory due to some disagreements with the real data.

Turker and San (2003) used pre- and post-event SPOT HRV images to detect the Izmit earthquake induced changes. The change areas were detected by subtracting the near-infrared channel of the merged pre-event image from that of the post-event image. The overall accuracy for the change areas were found to be 83%.

## CHAPTER 3

### BUILDING DAMAGE DETECTION USING WATERSHED SEGMENTATION

In this chapter, detection of the collapsed buildings from aerial photographs using the watershed segmentation algorithm is given. To do that, a technique was developed based on building shadows and image segmentation. The first part contains the explanation of the methodology. Then, each item in the methodology is examined in detail. This is followed by the presentation of the results.

#### 3.1. The Methodology

The main steps followed in the proposed building damage assessment method are shown in Figure 3.1. As seen in the flowchart, the post-event aerial photograph of the study area and the vector building boundaries were used as the inputs for the method. Initially, the post-event aerial photo was visually enhanced using histogram equalization technique to provide better discrimination between the buildings and their shadows. The effect of the preprocessing is illustrated on a small section of the study area in Figure 3.2. Next, the buildings were selected one-by-one using the raster data (aerial photo of the region) together with the vector data (vector building boundaries). Then, for each building, the shadow-producing edges were determined by means of a simple algorithm. To do that, the illumination angle, which was available from a previous study conducted by San (2002), was used. After finding the shadow edges, a buffer zone was generated along the shadow edges of the buildings. This was followed by the execution of the

watershed segmentation algorithm. For each building, a binary-colored output representing the shadow and non-shadow areas was generated. Finally, the accuracy assessment was carried out.

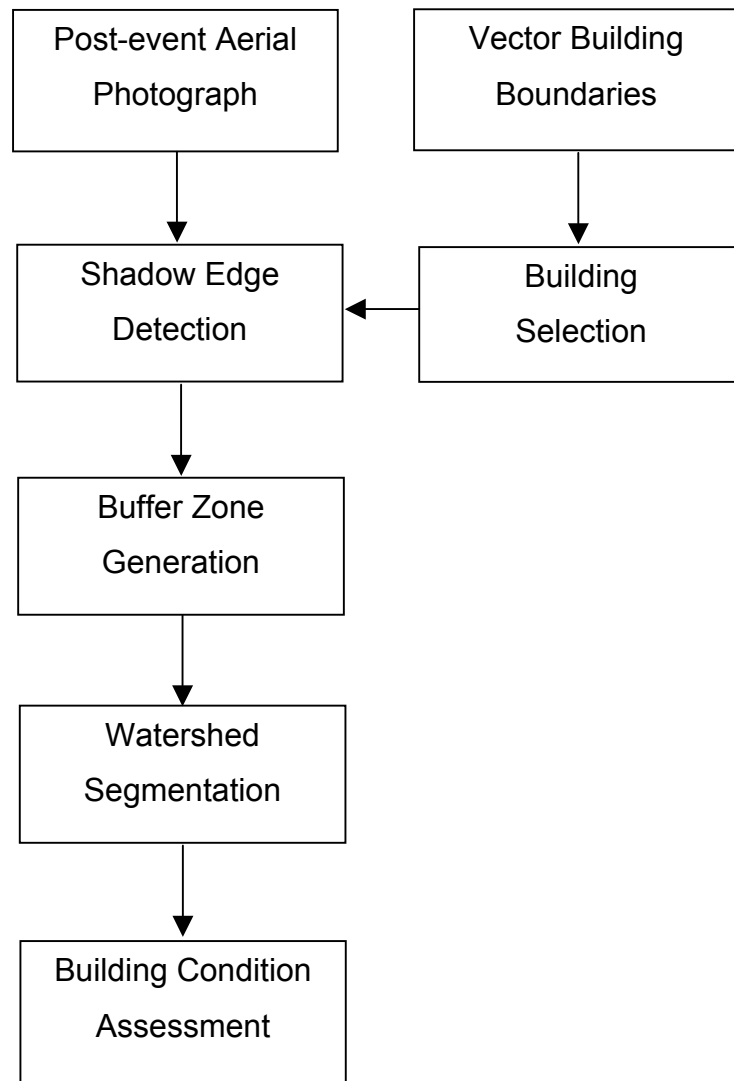


Figure 3.1. Damage detection using watershed segmentation

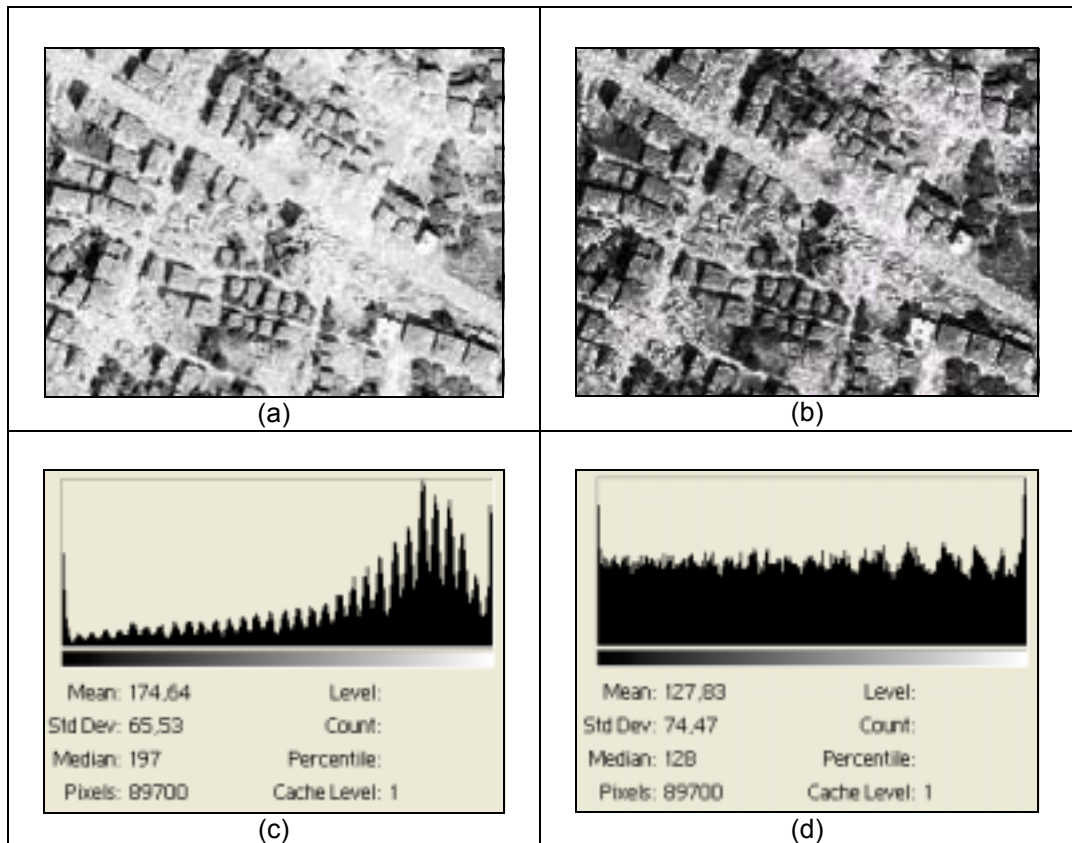


Figure 3.2. (a) Original aerial photo, (b) histogram-equalized aerial photo, (c) histogram of the original aerial photo, (d) histogram of the histogram-equalized aerial photo

### 3.2. Building Selection

To select the vector building polygons, each polygon was assigned a unique identification code between 1 and 284. Furthermore, the edges of each polygon were also given numerical codes between 1 and 4. Only four numbers were used while labeling the edges because in the study area, all the buildings were rectangular shaped. The labeled edges and the corresponding (x, y) coordinates of a building (#175) are illustrated in Figure 3.3. The labeling of the edges was necessary to identify the shadow casting edges of a building being assessed and to relate these edges with the corresponding cast shadows.

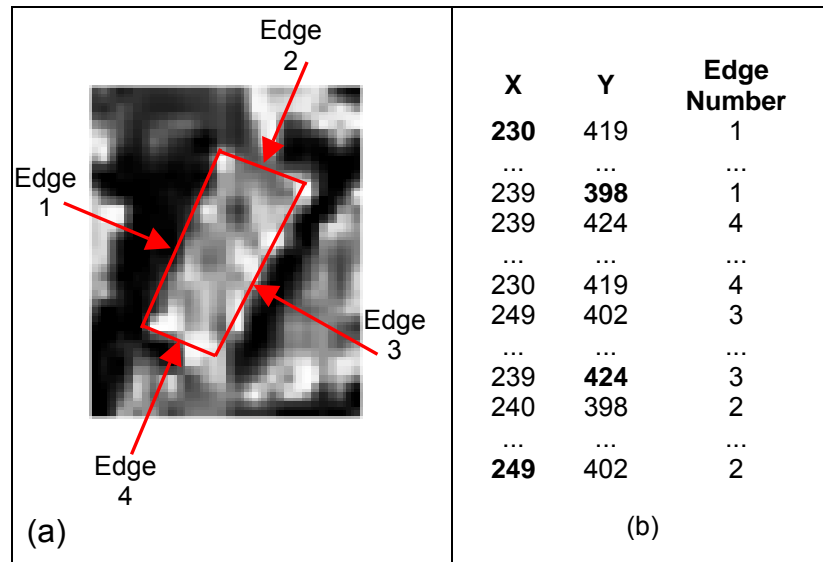


Figure 3.3. (a) The edges of building #175 and (b) the structure of vector data

After selecting a building, a minimum-bounding rectangle was created using the vector building boundary information by means of finding the minimum and maximum x-y coordinates (totally four values) in the table (Figure 3.3-b) that contains the coordinate values. According to the data presented in the table, minimum and the maximum (x,y) coordinates were found to be 230,398 and 249,424, respectively. Then, these points were connected to each other and a minimum-bounding rectangle was formed. A buffer bound was then generated around the minimum-bounding rectangle by expanding the resulting polygon about six pixels in all directions. This buffer was created in order to take the shadow regions produced by the buildings into consideration. The minimum bounding rectangle and the buffer bound generated on building #175 are illustrated in Figure 3.4.

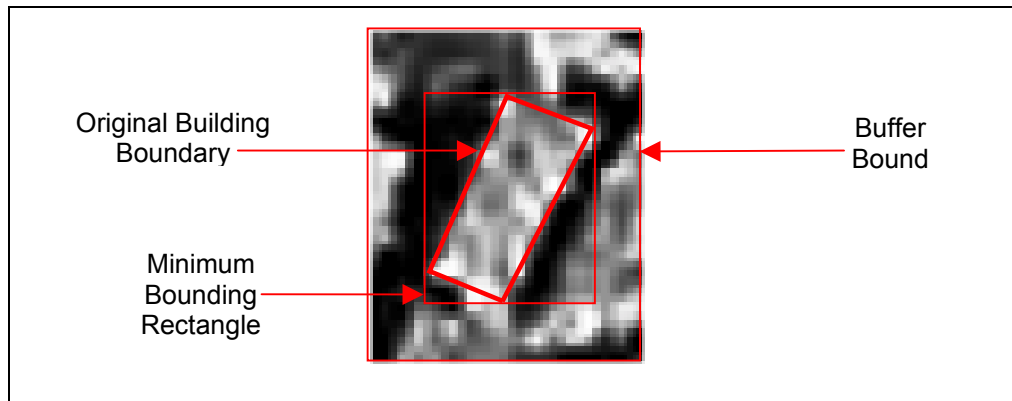


Figure 3.4. Minimum bounding rectangle and the buffer bound generated on building # 175

### 3.3. Shadow Edge Detection

The next step was the determination of the shadow edges for each building. The shadow producing edges were detected by using a simple algorithm, shown below:

---

```
for all buildings
    compute the corner points.
    find the distance between each corner point and the point located at
    the bottom right corner of the minimum bounding rectangle.
    sort the computed corner point distances.
    if there is one maximum distance
        then two shadow edges are computed.
        else if there is two maximum distances
            then one shadow edge is computed.
    end if
end for
```

---

In the algorithm, first, the corner points are found from the vector information. This is simply finding the points that share the same end point on adjacent edges. For instance, since both edge 4 and edge 1 share the same end point, that is  $(x,y) = (230,419)$ , this end point is selected as a corner point (Figure 3.3-b). Then, the Euclidean distances ( $d_1, d_2, d_3, d_4$ ), shown in Figure 3.5-a are computed between the corner points of the building and the corner of the minimum-bounding rectangle in the illumination direction. Next, the computed distances are sorted and the maximum or maximums are determined. If there is only one maximum distance, the edges that contain the same corner point are selected as the shadow edges. If, on the other hand, there are two maximum distances then, the edge that contains those corner points is labeled to be the shadow edge. These two cases can be illustrated with an example. If  $d_1 > d_4 > d_2 > d_3$ , then the shadow edges are determined as edge 1 and edge 2 (Figure 3.5-a). This is because the corner point connecting these edges possesses the farthest distance ( $d_1$ ). If the ranking is  $d_1 = d_4 > d_2 > d_3$ , then, edge 1 is selected as the shadow edge since it is the only edge containing the farthest distances  $d_1$  and  $d_4$ .

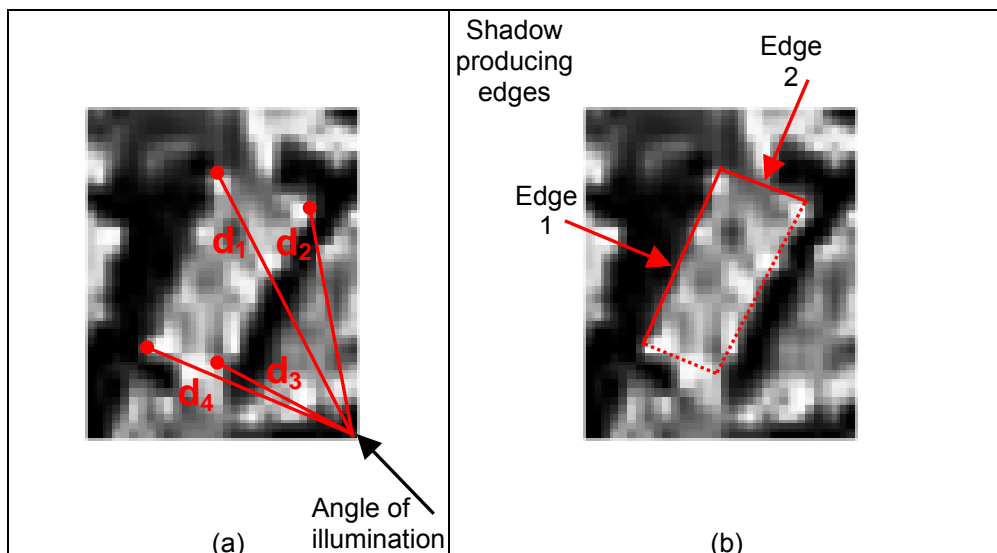


Figure 3.5. (a) The Euclidean distances ( $d_1, d_2, d_3$  and  $d_4$ ) and the angle of illumination, (b) the shadow producing edges of building # 175

### 3.4. Buffer Zone Generation:

The determination of the shadow producing edges was followed by the generation of a buffer zone. A three-pixel wide buffer area, inside and outside the building polygon, was generated around the shadow producing edges of each building (Figure 3.6). The inside building part of the buffer zone (zone B) was used for building analysis while the outside building part of the buffer zone (zone S) was used for shadow analysis. The purpose of the buffer zone generation was to deal with the shadow and building areas around the shadow producing edges of the buildings. These areas can also be called ‘the most significant parts’ of a building for the damage assessment.

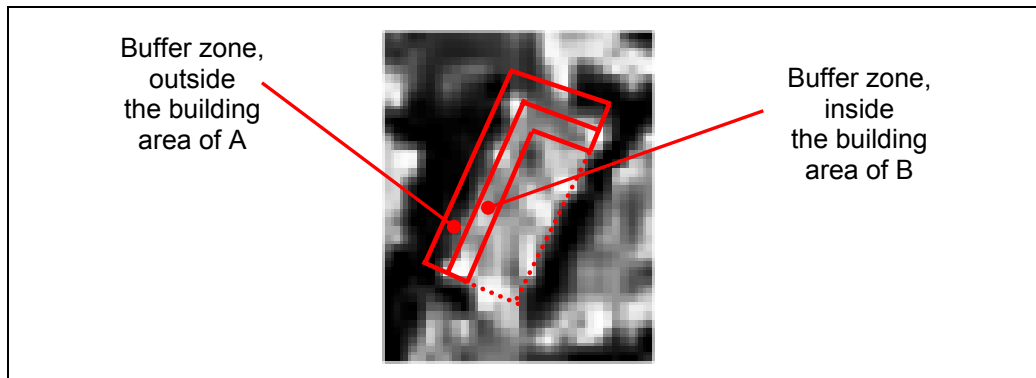


Figure 3.6. Buffer zone generation along the shadow producing edges

### 3.5. Watershed Segmentation:

This segmentation is based on the concepts of watersheds and catchment basins, which are well known in topography. In this approach, a gradient image can be regarded as a topographic surface where the gray-levels of the gradient image represent altitudes (Figure 3.7). Therefore, the edges in the image having high brightness values are considered as watershed lines while the interior regions of the image having low brightness values can be considered as catchment basins (Sonka et al. 1998).

The first step of the segmentation is finding the minima (catchment basin) and piercing of it. Then, whole relief is immersed into the water that causes the water flooding into the areas close to the piercing points. As the relief goes deeper in the water, some flooded areas tend to merge. In order to prevent this, infinitely tall dams are placed along the watershed lines. At the end, the resulting group of dams defines the watersheds of the image (Shafarenko *et al.* 1997). Vincent *et al.* (1991) developed a fast and flexible algorithm for computing watersheds in digital grayscale images. The algorithm is based on an analogy of an immersion process. In this algorithm, the flooding of the water in the image is efficiently simulated using a queue of pixels. They applied the algorithm in several fields with regard to picture segmentation including MR imagery and digital elevation models.

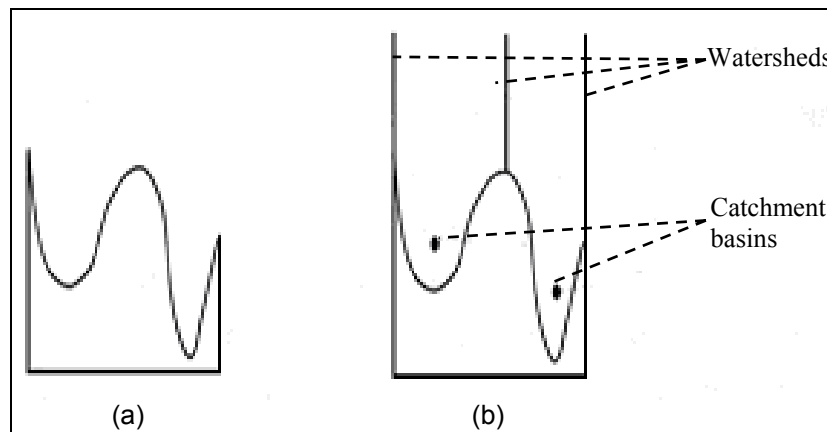


Figure 3.7. Watershed segmentation in one dimension: (a) gray-level profile of the image data; (b) watershed segmentation – local minima of gray level (altitude) yield catchment basins; local minima define the watershed lines.

In this study, the watershed segmentation was performed based on the idea of flooding from selected sources (Beucher *et al.*, 1992). These sources represent the markers. Two different markers were defined, one for shadow regions and the other for the building areas. These markers were utilized to avoid the over-segmentation, which is the situation that the watershed

segmentation algorithm finds too many unnecessary classes than needed. After the gradient image was found, the shadow and the building markers were selected within the outside building buffer zone (S) and the inside building buffer zone (B) respectively. The locations and the number of the markers were seeded randomly. Figure 3.8-a shows an example for the marker orientation on a gradient image.

The watershed segmentation algorithm was executed to generate a binary colored image. After running the watershed algorithm, the two-region output image was obtained. Of these regions, one refers to shadow areas while the other corresponds to the building areas. In Figure 3.8-b, the shadow and the building areas are shown in blue and yellow colors, respectively.

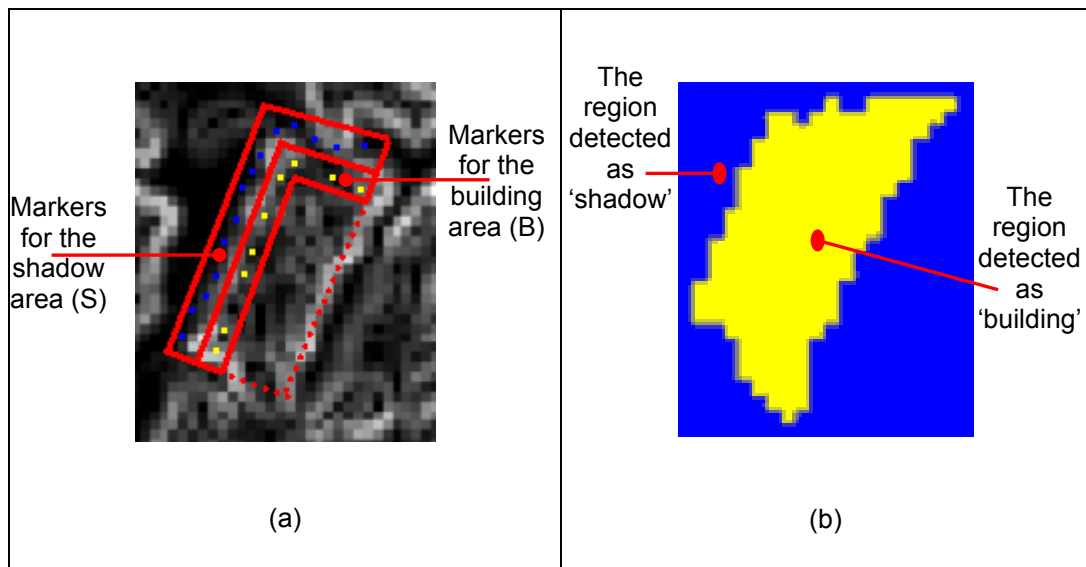


Figure 3.8. (a) The starting pixels (markers) for watershed transform, and (b) the segmented output after the watershed transform.

### 3.6. Building Condition Assessment

After detecting the shadow and building areas, the agreement was measured, for each building, within the buffer zone of the shadow producing edges between the pixels labeled as building and the pixels labeled as shadow (Figure 3.9). To do that the pixels inside the shadow buffer (S) and the building buffer (B) were counted and categorized as shadow or building pixel. Then, a ratio was computed between those pixels labeled as building and the total number of pixels falling inside the building region of the buffer zone. Similarly, a ratio was also computed between those pixels labeled as shadow and the total number of pixels falling inside the shadow region of the buffer zone.

This can be illustrated with an example. The pixel distribution of building # 175 is shown in Table 3.1. For this building, the shadow detection algorithm detected two shadow edges that are 1 and 2. The total number of pixels falling inside the buffer zone along the shadow edges were calculated and named as “Total Assessed Pixels” (Table 3.1). Totally, 99 pixels were generated for shadow buffer and 99 pixels were generated for building buffer. After performing the watershed transform, 91 shadow pixels (blue pixels) fell into the shadow buffer and 66 building pixels (yellow pixels) fell into the building buffer. Then, the building and the shadow ratios were calculated as  $66/99 = 66.67\%$  and  $91/99 = 91.92\%$ , respectively.

A user-defined threshold was used to make a decision about the condition of the building. If the building ratio or the shadow ratio was below the defined threshold value then, the building was labeled collapsed. If on the hand, both the building and the shadow ratios are over the defined threshold value then, the building was labeled un-collapsed. In deciding the building condition, the building and the shadow ratios were used together in order to avoid or reduce the misdetection of the buildings.

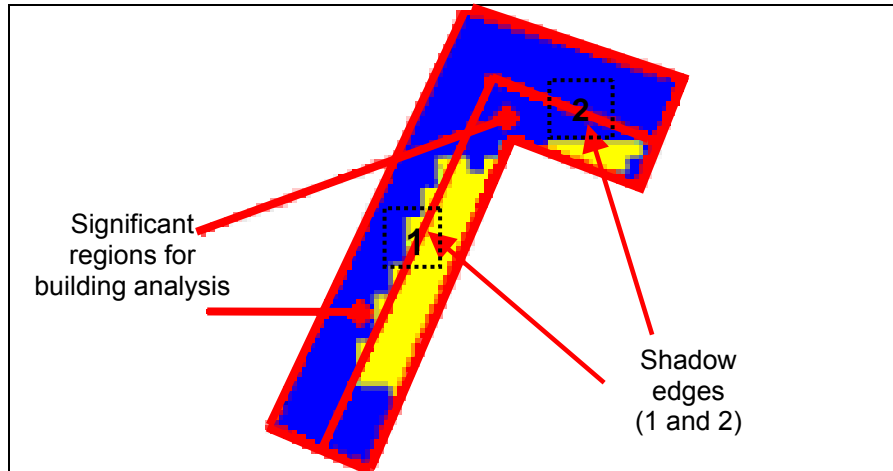


Figure 3.9. The shadow and building regions used in the assessment of the building condition.

Table 3.1. The calculation of (building / shadow) pixel ratios for building # 175.

Total Assessed Pixels: <b>99</b>
Detected Shadow Pixels: <b>91</b>
Detected Building Pixels: <b>66</b>
Shadow Ratio: <b>0.9192</b>
Building Ratio: <b>0.6667</b>

### 3.7. The Results

In this section, the results of the proposed damage analysis technique are presented. First, the optimum threshold level for building analysis is determined. Then, using the optimum threshold value, the computed results are provided by means of an error matrix. The summary of the whole process is illustrated in Figure 3.10.

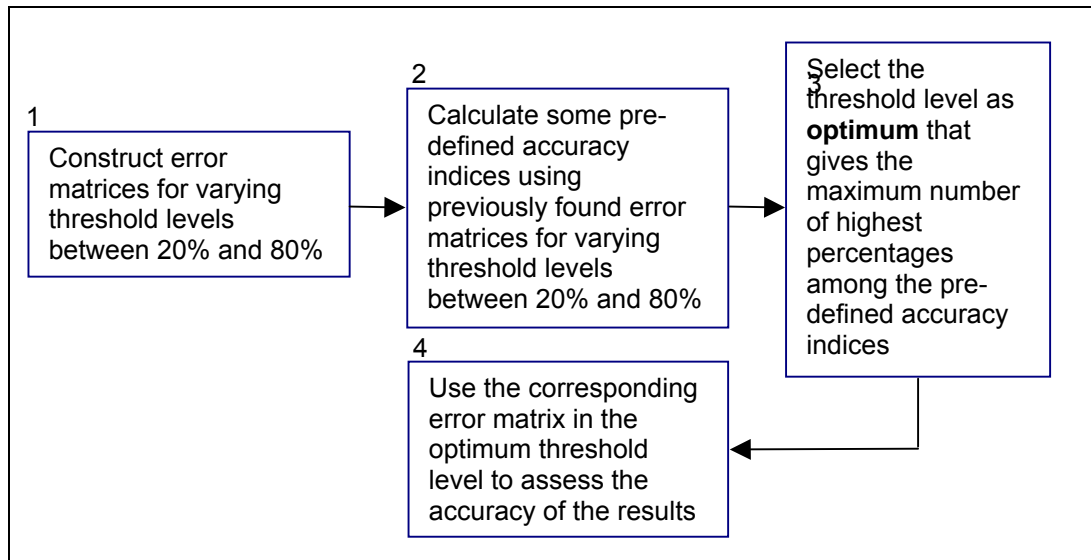


Figure 3.10. The process of optimum threshold determination and accuracy assessment

Error matrices were constructed for the threshold values of 20%, 30%, 40%, 50%, 60%, 70% and 80% (Appendix A). Then, by using these error matrices, the pre-defined accuracy indices, such as the overall accuracy, overall kappa, average user's accuracy, average producer's accuracy, combined user's accuracy and combined producer's accuracy were calculated (Table 3.2). The producer's accuracy indicates the probability of a reference building being correctly labeled and is a measure of omission error. On the other hand, the user's accuracy is the probability that a building labeled on the map actually represents that class on the ground truth data. Moreover, it is a measure of commission error (Story and Congalton, 1986). This table was then analyzed for determining the optimum threshold level (Fung and LeDrew, 1988), to be used in damage assessment of the buildings.

Table 3.2. The accuracy indices for the threshold values between 20% and 80%.

Threshold (%)	Overall Accuracy (%)	Overall Kappa x 100	Average Accuracy		Combined Accuracy	
			User's	Producer's	User's	Producer's
20%	72,89	4,71	73,93	51,66	73,41	62,28
30%	76,06	22,24	77,40	58,52	76,73	67,29
40%	77,46	35,32	73,09	65,33	75,28	71,40
50%	80,63	51,19	75,93	75,30	78,28	77,97
60%	74,65	45,01	71,41	75,83	73,03	75,24
70%	64,08	32,98	68,15	72,01	66,12	68,05
80%	42,61	11,28	62,98	59,08	52,80	50,85

As an example, the calculation of the accuracy indices, for an error matrix constructed at the 50% threshold level (Table 3.3), is given below. The calculations of the accuracy indices for the remaining threshold levels are given in Appendix B.

Table 3.3. The error matrix for the threshold value of 50%

	Reference		
	Collapsed	Un-collapsed	Total
Collapsed	50	26	76
Un-collapsed	29	179	208
Total	79	205	284

➤ Overall Accuracy =  $(50 + 179) / 284 * 100 = 80,63\%$

➤ Overall Kappa =  $(a_{\text{overall}} - a_{\text{observed}}) / (1 - a_{\text{observed}})$ ,

$$a_{\text{observed}} = \frac{(79 * 76) + (208 * 205)}{(76 * 79) + (76 * 205) + (79 * 208) + (205 * 208)} = 0.5119$$

➤ User's accuracy for collapsed buildings =  $50 / 76 * 100 = 65,79\%$

- User's accuracy for un-collapsed buildings =  $179 / 208 * 100 = 86,06\%$
- Average user's accuracy =  $(65,79 + 86,06) / 2 = 75,93\%$
- Producer's accuracy for collapsed buildings =  $50 / 79 * 100 = 63,29\%$
- Producer's accuracy for un-collapsed buildings =  $179 / 205 * 100 = 87,31\%$
- Average producer's accuracy =  $(63,29 + 87,31) / 2 = 75,30\%$
- Combined user's accuracy = (Overall accuracy + Average user's accuracy) / 2 =  $(80,63 + 75,93) / 2 = 78,28\%$
- Combined producer's accuracy = (Overall accuracy + Average producer's accuracy) / 2 =  $(80,63 + 75,30) / 2 = 77,97\%$

Of the six indices provided in Table 3.2, four gave the highest percentage (highlighted in gray) in the 50% threshold level. The remaining two indices did not reach to the maximum value at 50% due to the imbalance between the number of collapsed and un-collapsed buildings that are 79 and 205 respectively. However, their percentages were not quite different from the maximum. For this reason, 50% level was chosen as the optimum threshold.

The trend of the overall accuracies versus varying threshold values is also shown graphically in Figure 3.11. It can be clearly seen in the figure that the peak of the overall accuracy (80,63%) is reached when the threshold value is 50%. The shape of the curve is a little bit far from an ideal bell curve due to the difference in the number of collapsed and un-collapsed buildings.

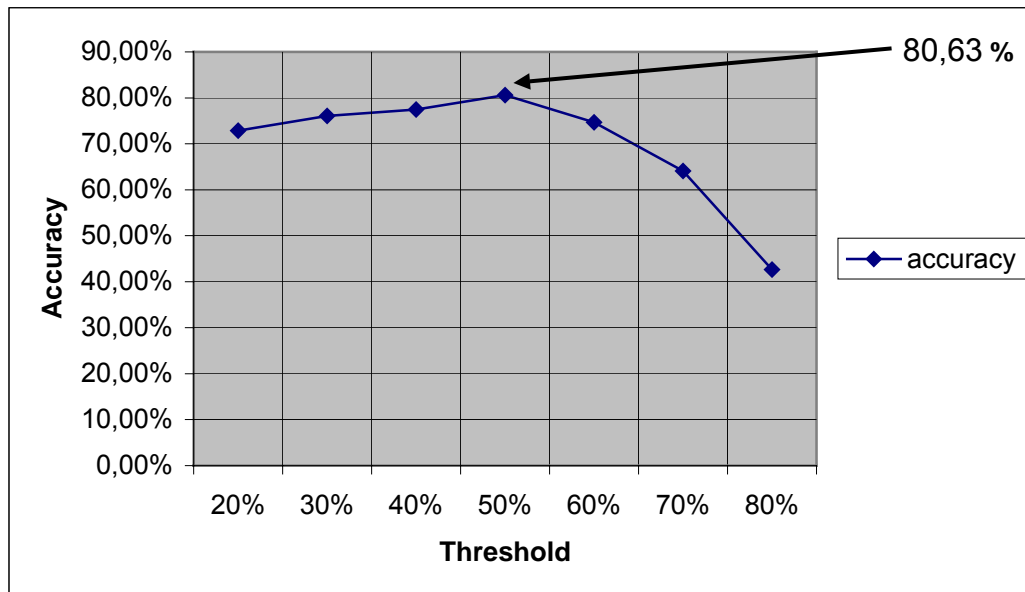


Figure 3.11. The change of the overall accuracy as the threshold changes.

Thus, all the buildings contained within the study area were analyzed using the optimum threshold of 50%. Of the 284 buildings, 229 were correctly detected by the proposed method. An error matrix was generated for the optimum threshold level by comparing the analysis results with the reference data. The error matrix contains the overall accuracy, the user's, and the producer's accuracies for collapsed and un-collapsed buildings (Table 3.4).

The overall accuracy (80,63%) was computed by dividing the sum of the diagonal of the error matrix (highlighted in gray) by the total number of the buildings (284). The producer's accuracy for collapsed and the producer's accuracy for un-collapsed buildings were computed to be 63,29% and 87,31%, respectively. On the other hand, the user's accuracy for collapsed and the user's accuracy for un-collapsed buildings were found to be 65,79% and 86,06%, respectively. It is evident from the results that, 55 buildings were incorrectly detected. Of these buildings, 29 were not detected as collapsed through the analysis. Instead, 26 un-collapsed buildings were detected as collapsed. The mis-detected buildings represent the omission and commission errors respectively.

Table 3.4. The error matrix for the optimum threshold value of 50% with accuracies

	Reference		
	Collapsed	Un-collapsed	Total
Collapsed	50	26	76
Un-collapsed	29	179	208
Total	79	205	284
Producer's Accuracy	63,29	87,31	
User's Accuracy	65,79	86,06	
Overall Accuracy	<b>80,63</b>		

## CHAPTER 4

### **BUILDING DAMAGE DETECTION USING BUILDING INTENSITY-GRADIENT ORIENTATION APPROACH**

The detection of the collapsed buildings using watershed segmentation was explained in the previous chapter. In this chapter, a new approach developed for detecting the collapsed buildings from aerial photographs based on building intensity and the orientation of the gradient is described. Initially, the methodology is introduced. Then, the explanation of the approach is followed. In the final section of the chapter, the results of the methodology are presented.

#### **4.1. The Methodology**

The proposed two-way building damage detection technique called “Building Intensity and Gradient Orientation” is illustrated in Figure 4.1. The word “intensity” refers to the intensity of the light reflected by the building. As in the watershed segmentation approach, discussed in the previous chapter, the post event aerial photo of the region and the vector boundary boundaries were used as the input data. Besides, the selection of the buildings was also performed by making use of the aerial photo and the vector data. Starting from this point, the detection process was divided into two branches. In the first branch, the detection process was performed based on building intensity information. To do that, an intensity threshold was determined by using the reference data and afterwards, this threshold was applied to original building images. Then, based on the analysis of the thresholded building images each building was labeled collapsed or un-collapsed.

In the second branch, a group of manipulations were carried out in order to make a decision about the condition of a building. First, a preprocessing was carried out on each building in order to smooth the image. After that, the gradient of the smoothed image was used to produce x and y partial derivatives. Next, the orientation and the magnitude of the gradient were calculated by using the partial derivatives. Then, by using the orientation information, an optimum threshold level was determined for the standard deviation of the angle distribution of the building pixels. Finally, as in the first branch, using the determined threshold level, a decision was made about the condition of each building. In the building condition assessment step, the results of the two branches were combined and a final decision was made about the condition of a building. At the end, the accuracy of the results was computed using the reference data.

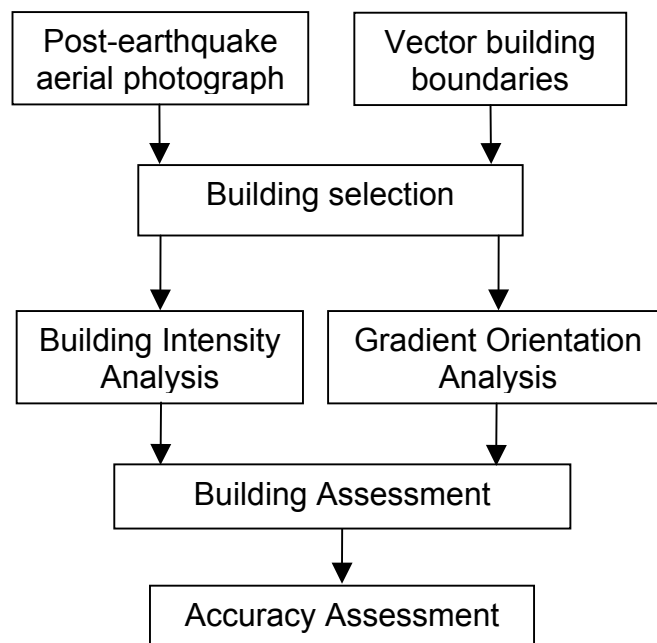


Figure 4.1. Damage detection using building intensity and gradient orientation analysis

## 4.2. Building Selection

Similar to watershed segmentation approach, the vector building boundary information was also used in this approach. To summarize: Each building polygon was assigned a unique identification number ranging between 1 and 284. Then, the edges of each building polygon were enumerated between 1 and 4 in the clock-wise direction (San, 2002). The main purpose for taking the vector data into account was to improve the accuracy of the building damage detection process by concentrating on building polygons only. In other words, the false alarm areas such as roads, grounds, vegetation and any other objects are eliminated.

After selecting a building, a one-pixel wide buffer region was generated by extending the building boundaries in all directions about one pixel. This region was created to improve the accuracy of building damage detection procedure. The main reasons for selecting the size of the buffer area no more than 1 pixel are twofold:

- the buffer area more than one pixel may increase the chance to include the unnecessary shadow areas in the analysis of the building under consideration, and
- the buffer area more than one pixel may increase the chance to include the undesired building and shadow areas of the neighboring buildings.

For above reasons, the false intensity values may be calculated during building intensity analysis. On the other hand, during the gradient orientation analysis, the angles of neighboring buildings may be involved or the standard deviation values may change due to the undesired regions.

In further analyses, the buffered buildings are also used together with the original ones to examine their differences in the accuracy. An example for an original and the buffered building is shown in Figure 4.2.

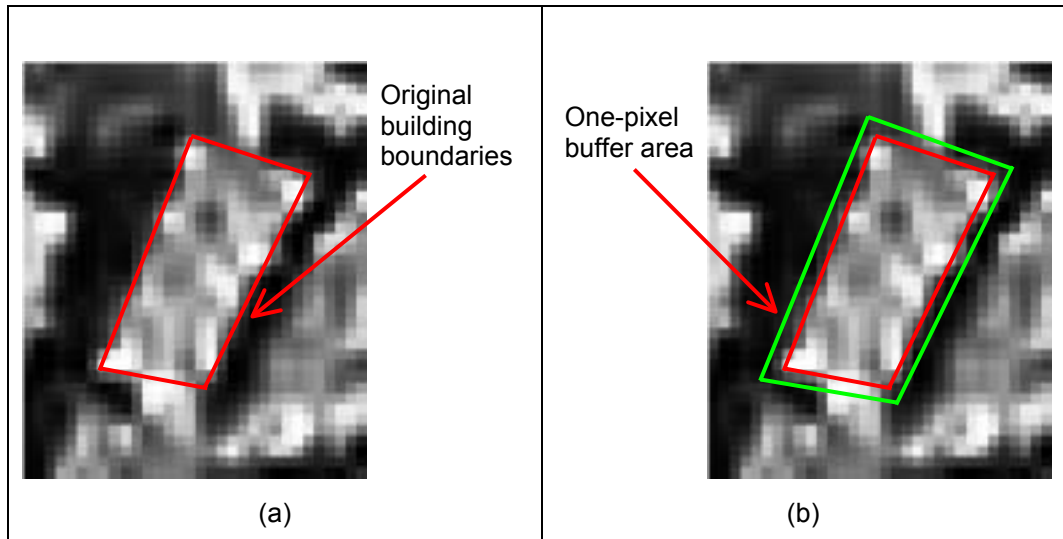


Figure 4.2. A building polygon (a) with no buffer area, (b) with a one-pixel buffer area.

### 4.3. The Building Intensity Approach

The motivation of this approach is to discriminate the collapsed and un-collapsed buildings based on brightness values inside the building polygons. In general, it was observed that the collapsed buildings reflect higher intensity values compared to un-collapsed buildings. The difference in the reflected brightness may be due to the roof type (mostly tile), appears dark in black and white, or some other objects located on the roofs that reduce the brightness value such as chimneys. In addition, the shadows caused by the slope of the roofs may also reduce the reflected intensity values for un-collapsed buildings. For these reasons, the amount of intensity reflected by different buildings may vary. In Figure 4.3, the intensity variation between a collapsed and an un-collapsed building is illustrated.

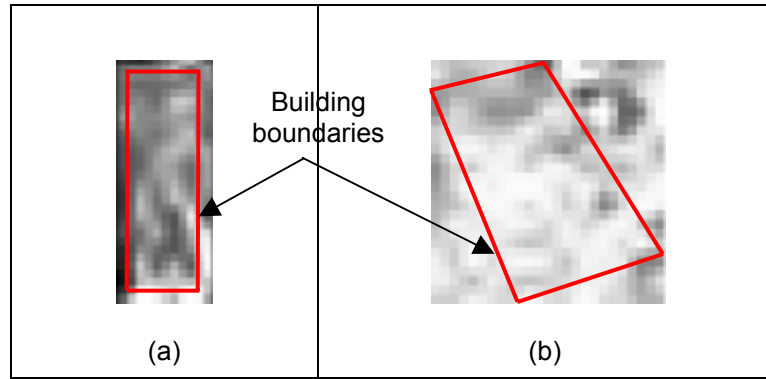


Figure 4.3. (a) An un-collapsed building with low intensity and (b) a collapsed building with higher intensity.

In the building intensity analysis, the first step was determining the intensity threshold level. In turn, this threshold level will be used to differentiate the collapsed buildings from the un-collapsed ones. The threshold value was determined through analyzing all the collapsed and un-collapsed buildings in the reference data by means of their brightness values. To find the exact threshold value, two different histograms were generated, one for collapsed and the other for un-collapsed buildings (Figure 4.4). Then, the intersection of the two normal curves, which gives the optimum intensity value, was found using the normalization curve equation shown below.

$$y = f(x | \mu, \sigma) = \frac{1}{\sigma(2\pi)^{1/2}} e^{-\frac{(x - \mu)^2}{2\sigma^2}} \quad -\infty < x < \infty \quad (\text{equation 1})$$

where,  $\mu$  is the mean value of the normal curve and  $\sigma$  is the standard deviation. In order to find the intersection of the two normal curves, the equation for collapsed buildings that have  $\mu = 171,3$  and  $\sigma = 25,27$  and the

equation for un-collapsed buildings that have  $\mu = 120,6$  and  $\sigma = 20,63$  were equalized.

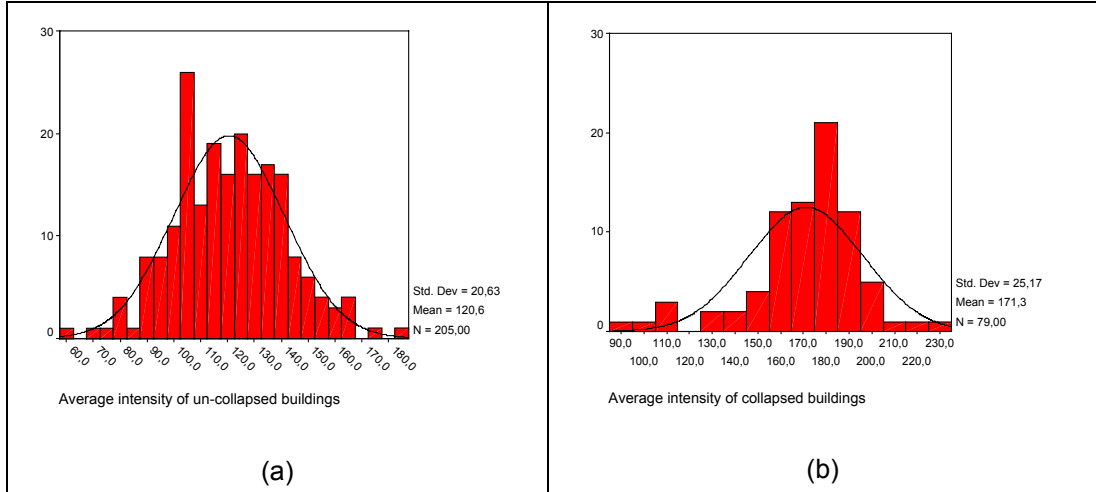


Figure 4.4. The intensity histogram for (a) un-collapsed buildings and (b) collapsed buildings.

After solving the two equations, the optimum intensity threshold level (value of  $x$  in the normalization equation) was found to be 145 (Appendix C). This simply means that those buildings collapsed due to earthquake will have an average intensity greater than 145. Therefore, this threshold value was applied to all buildings in the study area. A resultant image after applying the threshold value of 145 to a building is shown in Figure 4.5.

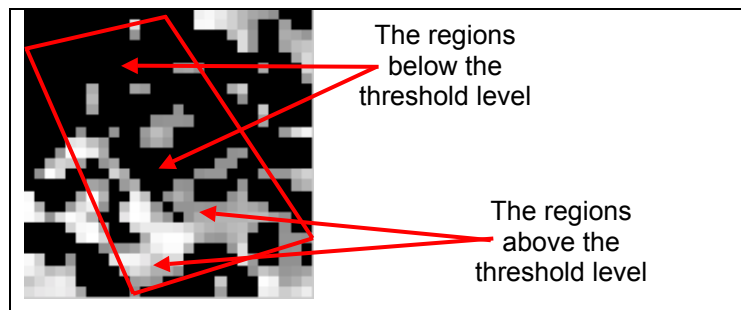


Figure 4.5. A building image after applying the threshold value of 145.

The same procedure was also carried out for all buildings that have one pixel wide buffer region. The intensity histograms generated for collapsed and un-collapsed buildings are illustrated in Figure 4.6.

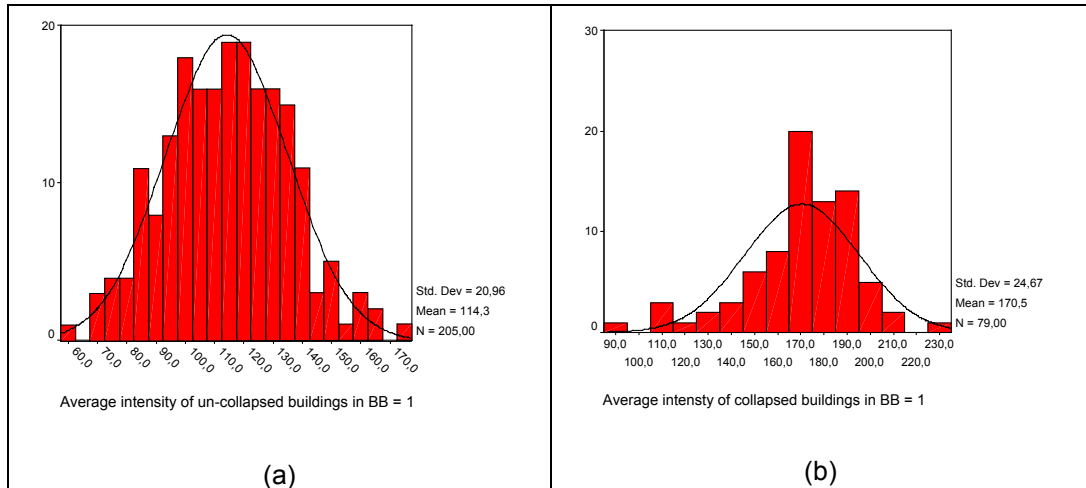


Figure 4.6. The intensity histograms for (a) un-collapsed buildings and (b) collapsed buildings that have one-pixel wide buffer bound.

Then, the two normalization curves were equalized in a similar way explained earlier and the intensity threshold level was calculated as 141 (Appendix D). This threshold level was also applied to the original image.

#### 4.4. The Gradient Orientation Approach

This approach is based on the detection of the variation in the gradient direction of the building image patches in order to discriminate the collapsed buildings from un-collapsed ones. It is assumed that, for collapsed buildings, the direction of gradient is randomly distributed. On the other hand, for un-collapsed buildings, the gradient orientation is assumed to be more regular and only slight variation in the angle is encountered (Figure 4.7). This assures that the discrimination of collapsed buildings from un-collapsed can

be achieved by analyzing the angle information of the gradient image of the buildings.

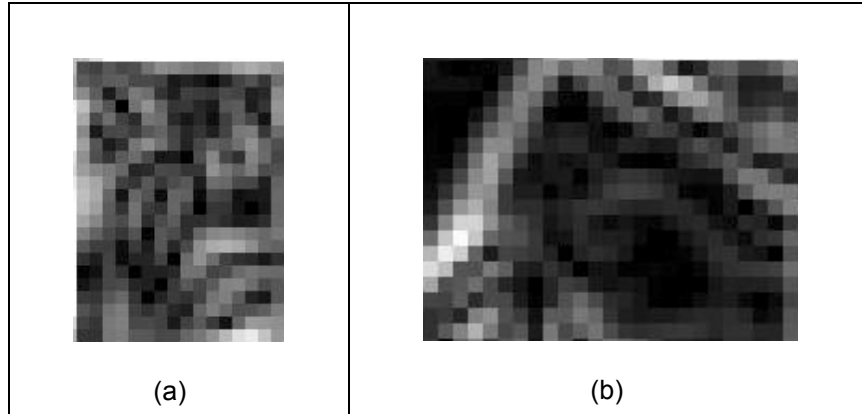


Figure 4.7. (a) A collapsed building with random gradient direction and (b) an un-collapsed building with regular gradient direction

#### 4.4.1. Image Pre-processing

The analysis of the gradient orientation was comprised of several steps. In the first step, the original building image patch was pre-processed using a Gaussian smoothing filter (equation 2), which suppresses the noise and controls the amount of detail in the building image:

$$G(x,y) = \frac{1}{2\pi\sigma^2} e^{-\frac{(x^2 + y^2)}{2\sigma^2}} \quad (\text{equation 2})$$

where,  $\sigma$  is the spread of the Gaussian and controls the degree of smoothing and  $(x,y)$  is a pixel within the filter window. The smoothed building image

patch,  $S(x,y)$ , was then generated after convoluting the original image,  $I(x,y)$ , using the Gaussian filter,  $G(x,y)$  (equation 3). The original and the smoothed building image patches are shown in Figure 4.8.

$$S(x,y) = G(x,y) * I(x,y) \quad \text{(equation 3)}$$

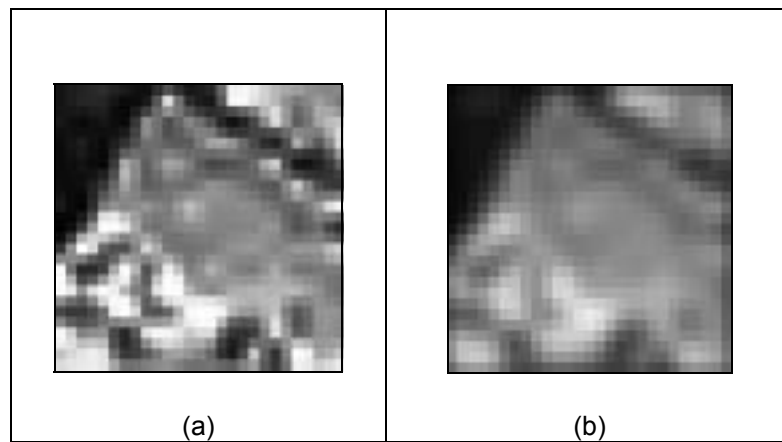


Figure 4.8. A building image patch (a) before smoothing and (b) after smoothing.

#### 4.4.2. The Calculation of the Gradient Orientation

In the next step, the smoothed image was utilized to produce the vertical and horizontal partial derivatives, which were computed by averaging the finite differences over a 2x2 square array (equation 4).

$$P(x,y) \approx (S(x,y+1) - S(x,y) + S(x+1,y+1) - S(x+1,y)) / 2$$

$$Q(x,y) \approx (S(x,y) - S(x+1,y) + S(x,y+1) - S(x+1,y+1)) / 2$$

(equation 4)

where,  $P(x,y)$  and  $Q(x,y)$  are the vertical and horizontal partial derivatives, respectively and  $S(x,y)$  is the smoothed image patch. Then, the magnitude and the orientation of the gradient were calculated using equation 5.

$$M(x,y) \approx (P(x,y)^2 + Q(x,y)^2)^{1/2} \quad \text{(equation 5)}$$

$$\theta(x,y) \approx \arctan (Q(x,y), P(x,y))$$

where,  $M(x,y)$  is the magnitude of the gradient,  $\theta(x,y)$  is the orientation of the gradient and  $\arctan(x,y)$  is a function that returns an angle between  $[-\pi, +\pi]$  (Lecture Notes on Image Processing Algorithms Course, 2002). But, in the present case, this range was then mapped into  $[0, +\pi]$  interval. As an example, the partial representation of the gradient magnitude and the orientation (for each pixel) of a building patch are shown in Figure 4.9, where, the numbers represent the angle values (between  $0^\circ$  and  $180^\circ$ ) of the corresponding pixels.

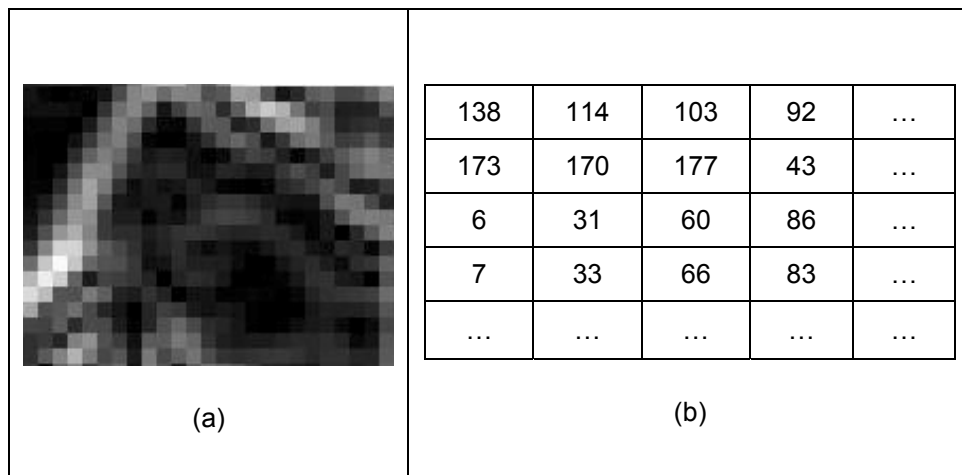


Figure 4.9. (a) The gradient magnitude and (b) the gradient orientation of a building patch

#### 4.4.3. Threshold Determination for the Optimum Standard Deviation

After obtaining the gradient orientation, the whole angle interval ( $0^{\circ} - 180^{\circ}$ ) were divided into  $15^{\circ}$  sub-intervals which were (1) 0-15, (2) 16-30, (3) 31-45, (4) 46-60, (5) 61-75, (6) 76-90, (7) 91-105, (8) 106-120, (9) 121-135, (10) 136-150, (11) 151-165 and (12) 166-180. Then, for each building, the gradient direction histograms were generated. In these histograms, the abscissa represents the gradient direction from 0 to 180 degrees divided into 12 equal intervals while the ordinate represents the frequency of the gradient directions. Figures 4.10-a and 4.10-b illustrate the histograms for a collapsed and an un-collapsed building, respectively.

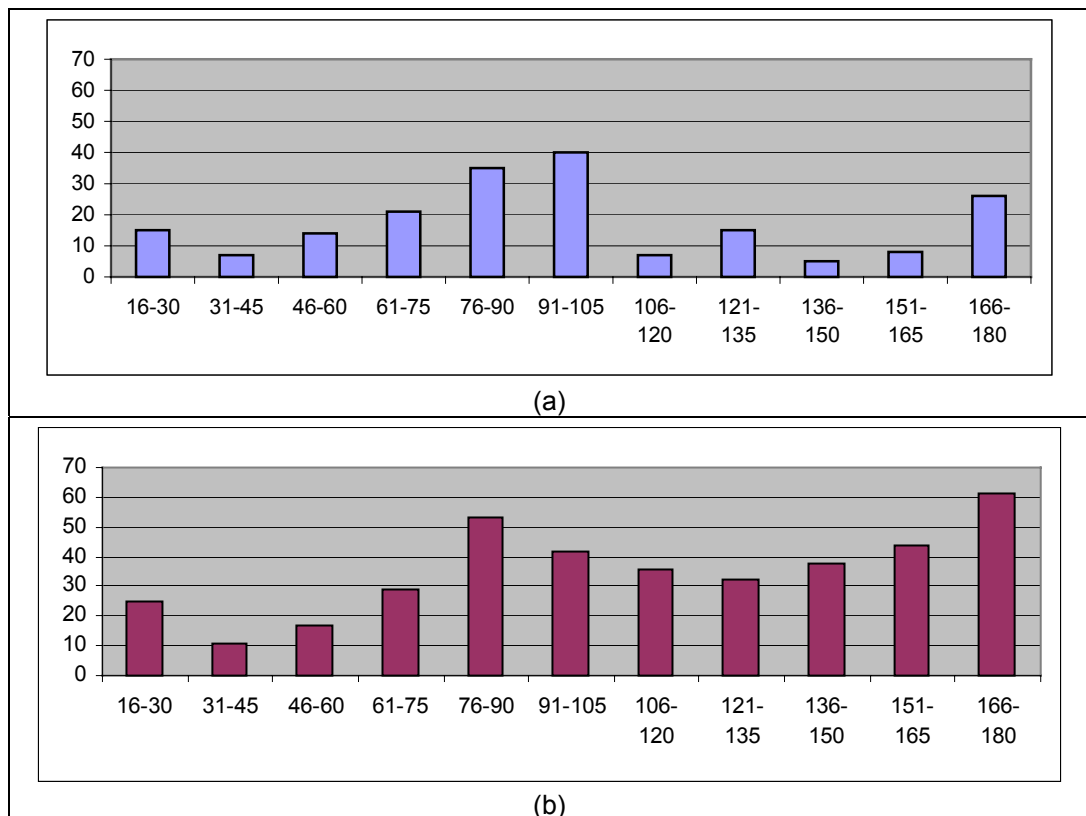


Figure 4.10. (a) An un-collapsed building and (b) a collapsed building with un-biased frequencies

As can be seen in the figure, the ( $0^{\circ} - 15^{\circ}$ ) interval was not taken into account due to its high frequency, which occurs a biased distribution. After eliminating this interval, the histogram of a collapsed building looks more-or-less flat when compared with the histogram of an un-collapsed building, which concentrates in one or two directions.

In the study area, the number of pixels falling within the building polygons (size of the buildings) was not the same for all buildings. For this reason, for each histogram, the frequency values were mapped into 0 – 100 interval proportional to the building size. At the end of this mapping process, the new histograms were constructed (Figure 4.11). This was followed by the calculation of the standard deviations of the new histograms. It was observed that most of the collapsed buildings have low standard deviation values due to their flat distribution. On the other hand, most of the un-collapsed buildings have high standard deviations.

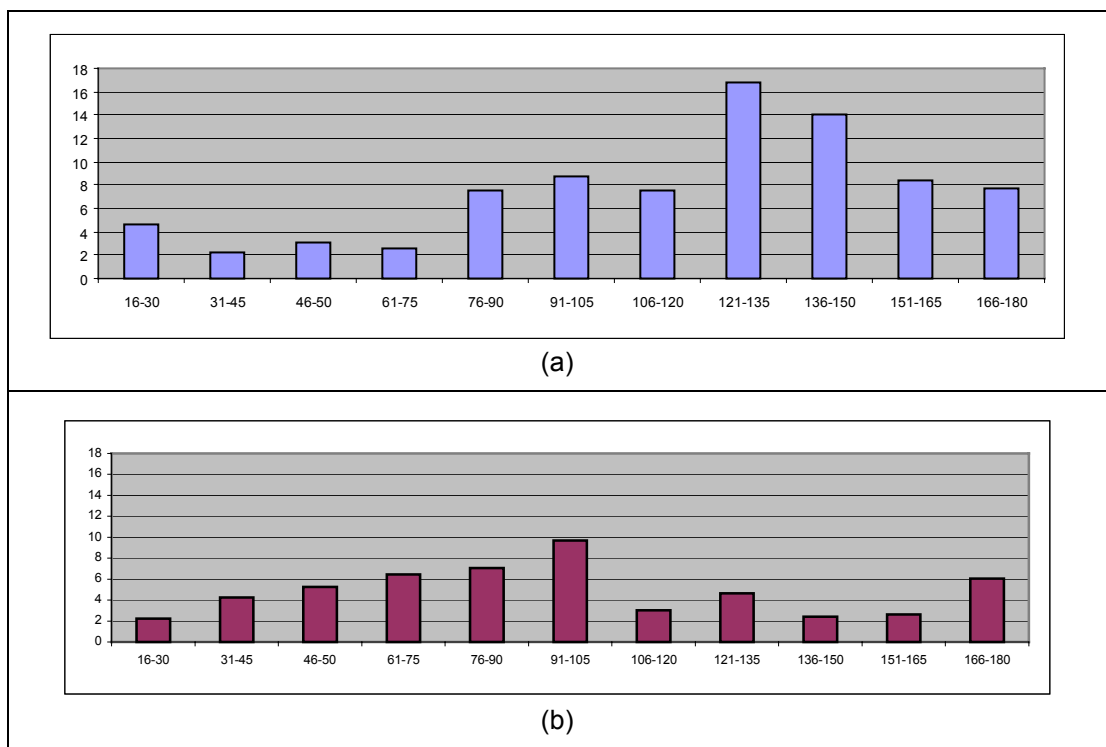


Figure 4.11. (a) An un-collapsed building and (b) a collapsed building with un-biased frequencies after mapping the frequency values between 0 and 100.

As a final step, the optimum standard deviation threshold that discriminates the collapsed buildings from the un-collapsed was determined. To do that, the average of the standard deviation values of all collapsed and un-collapsed buildings were computed. For collapsed and un-collapsed buildings, the computed values were found to be 16,07 and 17,93, respectively. Then, by applying the same procedure as in the optimum intensity threshold level determination in the previous section, an optimum threshold of 17 was found. The similar processes were also carried out for the one-pixel wide buffer region generated building polygons. In this case, the optimum standard deviation value was found to be 17,31.

#### **4.5. Assessments of the Conditions of the Buildings by Integrating Both Approaches**

After performing the building intensity analysis, the optimum intensity threshold was computed to be 145 for the buildings when a buffer zone is not generated and 141 when a one pixel wide buffer zone is generated. After that, for each building, those pixels having brightness values higher than the threshold were counted and then divided into the total number of pixels contained within the building. The result gave us the pixel ratio per building. This can be illustrated with an example. In Figure 4.5, the number of pixels staying above the optimum threshold level of 145 is 114 and the total number of pixels contained within this building is 256 pixels. Thus, the pixel ratio is computed to be  $114 / 256$  or 44,53 %.

In general, it was observed that the pixel ratios were higher for collapsed buildings than the pixel ratios for un-collapsed buildings. This is because, the pixels with high intensity values were much more present within collapsed buildings. As a consequence of the analysis, 60% pixel ratio was accepted to be the optimum threshold level that differentiates collapsed buildings from un-collapsed. Thus, those buildings having a pixel ratio greater than 60%

was labeled collapsed. Otherwise, the buildings were categorized as un-collapsed.

As mentioned above, in the gradient orientation approach, the optimum standard deviation threshold value was found to be 17. Therefore, this value was used to discriminate the collapsed buildings from the un-collapsed ones. If the standard deviation of a building's gradient direction histogram was below the optimum standard deviation then, the building was accepted to be collapsed. Otherwise, the building was labeled un-collapsed.

The final decision about the building condition was made by combining the results of the building intensity and the gradient orientation approaches. A building was marked collapsed if its pixel ratio was above the predefined pixel ratio of 60% **and** the standard deviation of its gradient direction histogram was below the optimum standard deviation of 17. On the other hand, a building was labeled un-collapsed if its pixel ratio was below the predefined pixel ratio of 60% **and** the standard deviation of its gradient orientation histogram was above the optimum standard deviation of 17. The similar processings were also carried out for the one-pixel wide buffer region generated building polygons. In this case, the pixel ratio of 60% was preserved but the optimum standard deviation value of 17 was changed to 17,31.

By using the optimum pixel ratio and the optimum standard deviation threshold value, the results were obtained. Then, for the assessment of the accuracy, an error matrix was created for; (i) the buildings without a buffer zone and (ii) the buildings with a buffer zone of 1 pixel. The main steps of the optimum pixel ratio determination and the accuracy assessment to get the results is given below:

- The error matrices for varying threshold levels between 10% and 90% were constructed.

- The predefined accuracy indices were computed using the previously constructed error matrices for varying pixel ratios.
- The optimum pixel ratio that gives the maximum number of highest percentages among the predefined accuracy indices was selected.
- The accuracy of the results was assessed by using the corresponding error matrix in the optimum pixel ratio.

#### 4.6. The Results

As listed at the end of the previous section, the error matrices for the varying pixel ratios changing between 10% and 90% were constructed. By using these matrices, several predefined accuracy indices including overall accuracy, overall kappa, average user's and producer's accuracies, and combined user's and producer's accuracies were computed (Table 4.1). In a similar way, a table for the buffered case was also generated (Table 4.2).

Table 4.1. The accuracy indices for the pixel ratios between 10% and 90%

Pixel Ratio (%)	Overall Accuracy (%)	Overall Kappa x 100	Average Accuracy %		Combined Accuracy %	
			User's	Producer's	User's	Producer's
10%	28,52	0,55	64,01	50,49	46,26	39,50
20%	34,51	5,38	64,91	54,63	49,71	44,57
30%	47,54	16,47	65,52	62,88	56,53	55,21
40%	64,79	35,06	69,72	73,66	67,25	69,23
50%	82,75	62,18	79,52	85,33	81,13	84,04
60%	89,44	73,70	86,85	86,85	88,14	88,14
70%	89,08	69,63	91,83	81,16	90,46	85,12
80%	80,99	40,06	89,58	65,82	85,28	73,40
90%	73,94	8,89	86,74	53,16	80,34	63,55

Table 4.2. The accuracy indices for the pixel ratios between 10% and 90% in the buffered case

Pixel Ratio (%)	Overall Accuracy (%)	Overall Kappa x 100	Average Accuracy %		Combined Accuracy %	
			User's	Producer's	User's	Producer's
10%	28,87	0,82	64,06	50,73	46,47	39,80
20%	34,86	5,67	64,96	54,88	49,91	44,87
30%	49,30	18,26	66,04	64,10	57,67	56,70
40%	65,85	37,19	71,04	75,17	68,44	70,51
50%	85,21	67,02	81,77	87,42	83,49	86,32
60%	90,85	76,84	89,08	87,82	89,96	89,33
70%	90,85	74,64	94,37	83,54	92,61	87,19
80%	81,34	41,46	89,73	66,46	85,53	73,90
90%	74,65	12,31	87,00	54,43	80,83	64,54

Of the six indices represented in Tables 4.1 and 4.2, four gave the highest percentage (highlighted in gray) in the 60% threshold level. The remaining two indices did not reach to the maximum at 60% threshold level although their percentages were not quite different from this peak value. The reason for this would be that there is a wide range between the number of collapsed and un-collapsed buildings.

The tendencies of the overall accuracies versus varying threshold levels for the un-buffered and buffered cases are shown in Figures 4.12 and 4.13, respectively. As can be seen from the figure that the peaks of the overall accuracies (89,44%) and (90,85%) are reached when the pixel ratio is 60%. The shape of the curve is a little bit far from the ideal bell curve similar to the results of watershed segmentation approach. This is because there exists an imbalance between the number of collapsed and un-collapsed buildings.

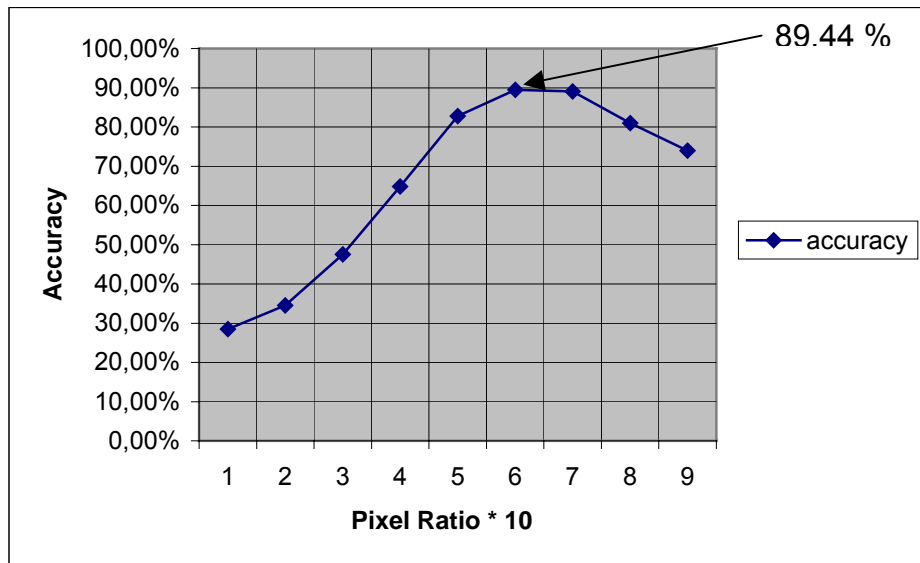


Figure 4.12. The change of the overall accuracy as the pixel ratio changes

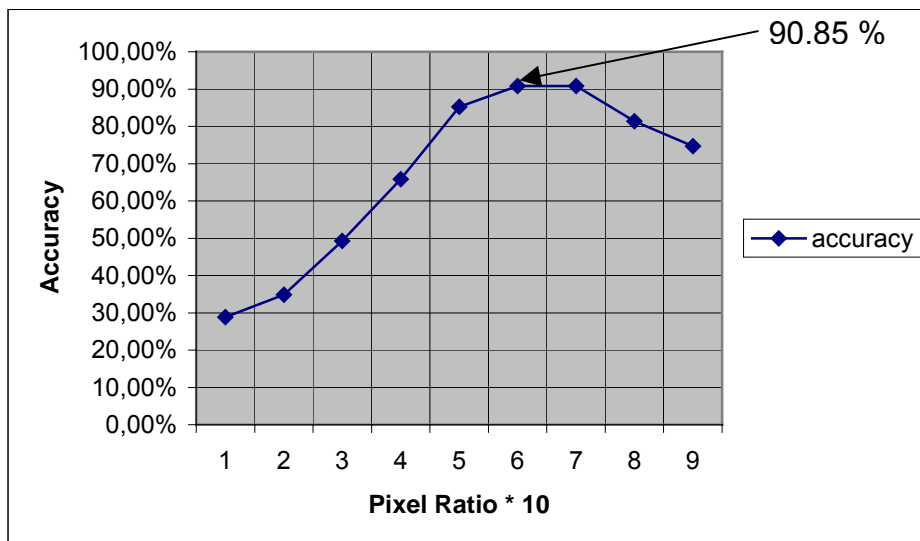


Figure 4.13. The change of the overall accuracy as the pixel ratio changes in the buffered case

Therefore, all the buildings in the study area were assessed using the pixel ratio of 60% and the optimum standard deviation threshold value of 17 (in the un-buffered case) and 17,31 (in the buffered case). Of the 284 buildings, 254 and 258 buildings were correctly detected in the un-buffered and buffered

cases, respectively by the integrated approach. The error matrices were generated using the optimum pixel ratios by comparing the analyzed results with the ground truth. The error matrices include the overall accuracy, the user's and the producer's accuracies for collapsed and un-collapsed buildings (Table 4.3 – 4.4).

Table 4.3. The error matrix for the optimum pixel ratio and standard deviation threshold levels in the un-buffered case

	Reference		
	Collapsed	Un-collapsed	Total
Collapsed	64	15	79
Un-collapsed	15	190	205
Total	79	205	284
Producer's Accuracy	81,01	92,68	
User's Accuracy	81,01	92,68	
Overall Accuracy	<b>89,44</b>		

Table 4.4. The error matrix for the optimum pixel ratio and standard deviation threshold levels in the buffered case

	Reference		
	Collapsed	Un-collapsed	Total
Collapsed	64	11	75
Un-collapsed	15	194	209
Total	79	205	284
Producer's Accuracy	81,01	94,63	
User's Accuracy	85,33	92,82	
Overall Accuracy	<b>90,85</b>		

The overall accuracies were calculated as 89,44% and 90,85% for the un-buffered and buffered cases, respectively. In the un-buffered case, both the user's and the producer's accuracies were computed, for collapsed buildings, as 81,01%. On the other hand, for un-collapsed buildings, both the user's and

the producer's accuracies were found to be 92,68%. In the buffered case, the producer's accuracies for collapsed and un-collapsed buildings were computed to be 81,01% and 94,63%, respectively. On the other hand, the user's accuracies for collapsed and un-collapsed buildings were computed to be 85,33% and 92,82%, respectively.

It can be observed that 30 buildings in the un-buffered case and 26 buildings in the buffered case were not detected correctly due to several reasons. In the un-buffered case, of the 30 mis-detected buildings, 15 were not detected as collapsed through the analysis. Instead, 15 un-collapsed buildings were detected as collapsed. In the buffered case, of the 26 mis-detected buildings, 15 were not detected as collapsed through the analysis. Instead, 11 un-collapsed buildings were detected as collapsed. In each case, the mis-detected buildings represent the omission and commission errors respectively.

## CHAPTER 5

### DEVELOPING A BUILDING DAMAGE DETECTION SOFTWARE

In this chapter, the software development part of the study is described. The chapter includes four main sections. First, the system design is explained. In this section, the functionalities of the software and the architecture of the system are introduced. Secondly, the watershed segmentation component of the software is presented. This is followed by the explanation of the second approach, building intensity – gradient orientation. Finally, the image analysis component is described.

#### 5.1. System Design

The building damage detection software was implemented using MATLAB®, which stands for **matrix laboratory**, a high-performance language mostly used for technical computing. It integrates computation, visualization, and programming in a user-friendly environment. Typical uses of Matlab are as follows:

- Mathematics and computation
- Algorithm development
- Data acquisition
- Modeling, simulation and prototyping
- Data analysis, exploration, and visualization

- Scientific and engineering graphics
  
- Application development, including graphical user interface building

MATLAB includes a group of add-on application-specific solutions called toolboxes. The toolboxes allow the user to learn and apply specialized technology and provide to solve particular classes of problems. Areas in which toolboxes are available include image processing, signal processing control systems, neural networks, fuzzy logic, wavelets, simulation, and many others. On the other hand, MATLAB possesses a system that includes many parts such as development environment, the MATLAB mathematical function library, the MATLAB language, graphics and, the MATLAB application program interface (API) (MATLAB 6.5.0 manual, 2002).

The motivation of the software development has arisen, from the need of automating the earthquake damage detection methods. This brings some advantages such as speed, easiness and compactness. The damage detection software works fast since all the operations are executed on a single environment. No other supplementary program is needed. In addition, it is easy to use the system due to its user-friendly structure supported by the graphical user interface (GUI). Finally, the system has a compact form that packs the two earthquake damage detection methodologies in a standalone environment. This property gives the opportunity of testing different methods on a single data and comparing the results of them.

The architecture of the developed system is illustrated in Figure 5.1. As can be seen in the figure two different inputs are fed into the system components that are the post-event aerial image and the vector building boundary information. The post-event aerial photograph is input to all the components of the software while the vector building boundaries are utilized by the image analysis component only. At the output side, two different outputs are

obtained from this earthquake damage detection system. The components other than the image analysis generate the labeled buildings, such as the collapsed or un-collapsed in a graphical or textual mode. On the other hand, image analysis component is used to generate visually enhanced image outputs. These processes include several image processing operations, such as image enhancement and edge detection.

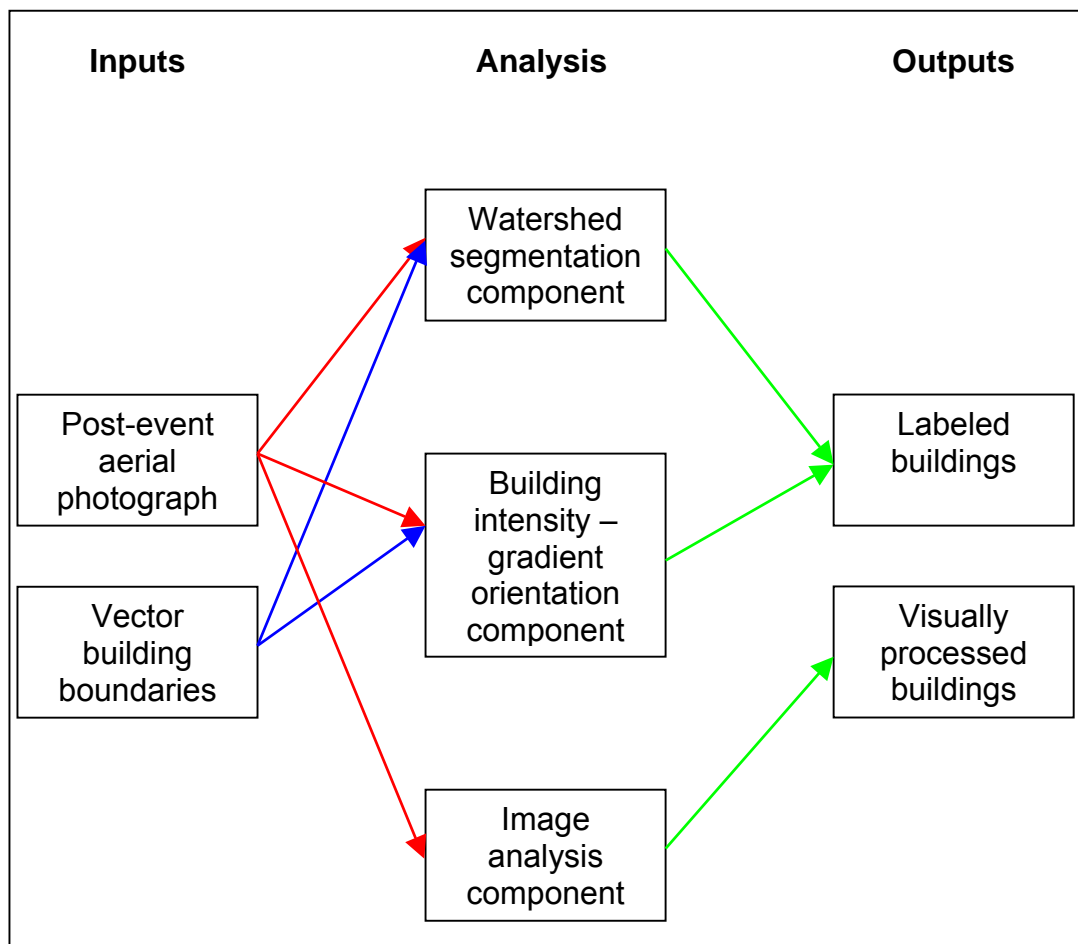


Figure 5.1. The architecture of the system

## 5.2. Watershed Segmentation Component

The watershed segmentation component of the system was designed to automatically detect the collapsed buildings from a post-event aerial photograph using the first approach. Therefore, to do that, all the processes mentioned in chapter 3 were implemented within this component. The source code of the watershed segmentation component can be seen in Appendix E.

The detection procedure starts with the determination of the method in the main window (Figure 5.2). To start the watershed segmentation approach, the upper radio button must be selected. Then, this choice is confirmed by clicking the 'Ok' button. The 'Exit' button is used for the termination of the program and the 'About' button gives information about the author and the version of the program, correspondingly.

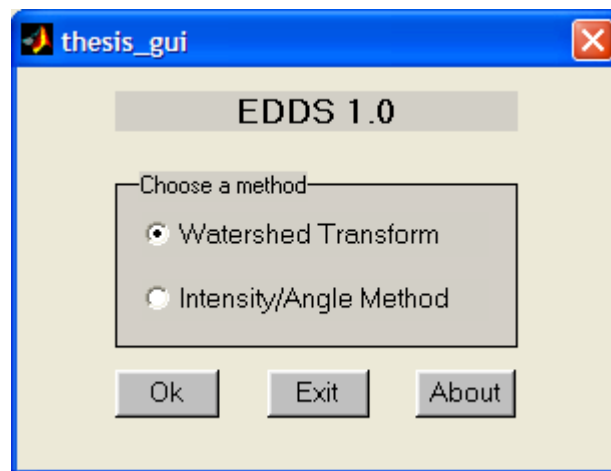


Figure 5.2. Main menu of the damage detection software

After selecting the method, a new window is displayed on the screen. This window contains several menu items, such as file, attributes, segmentation and image analysis (Figure 5.3). Except for the image analysis, the other menu items are examined below.

- File: This menu item comprises of two options: (i) Displaying the photograph of the study area and (ii) quitting the program.
- Attributes: Using this menu item, several adjustments can be carried out before performing the watershed segmentation. For example, the buffer bound, the buffer depth and the threshold value can be set. While the buffer bound and the buffer depth are scaled between 1 and 10 pixels, the threshold level gets a value between 0% and 100%. In the optimum case, the buffer bound is selected as 6 and the buffer depth (size of the buffer zone) is set to 3 pixels. On the other hand, the threshold level is determined as 50% (Figure 5.3).

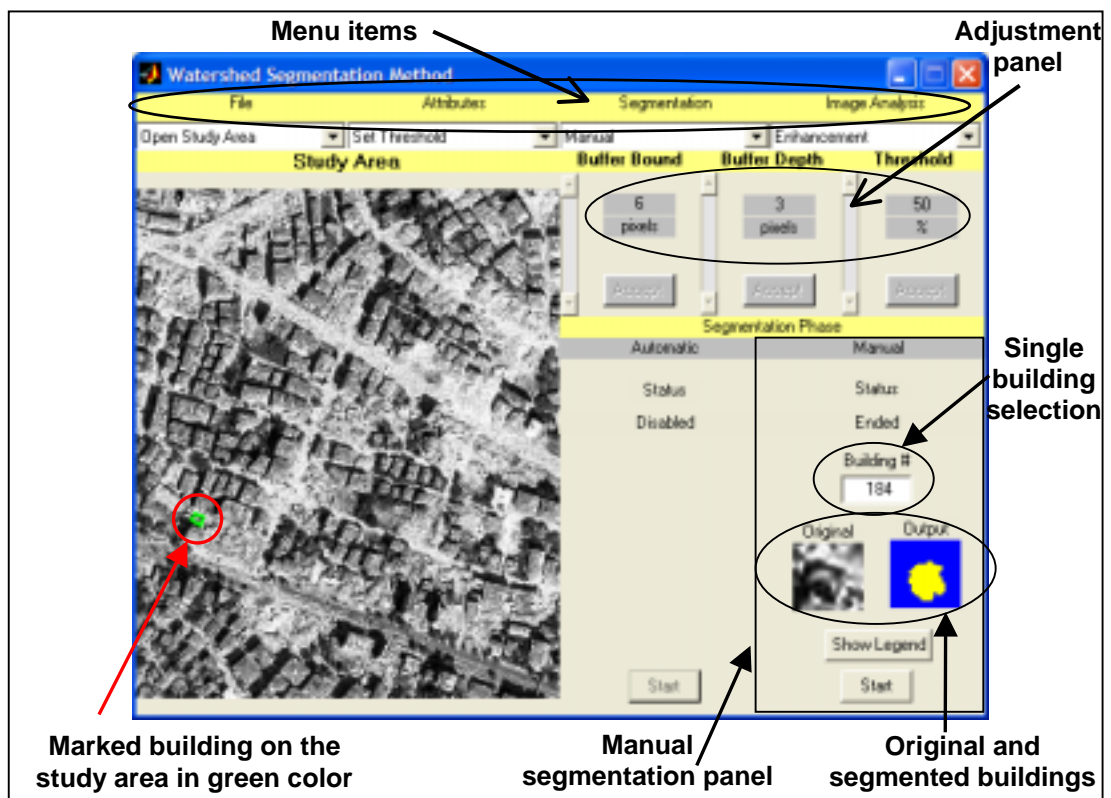


Figure 5.3. A general view of the watershed segmentation interface and the results of the manual segmentation

- Segmentation: In this menu item, the mode of the segmentation can be determined to be either (i) manual or (ii) automatic. In the manual mode, the building number is entered into the edit box manually and the 'start' button located in the manual segmentation panel is clicked. After this operation, the segmented building is displayed on a small window. In addition, the corresponding building is marked on the image by a color that represents its condition (Figure 5.3). Four different colors are used to represent the conditions of the buildings. According to the legend designed, green color represents that the building is un-collapsed. The red is used for collapsed buildings, while blue and yellow signify the omission and commission errors, respectively. In the example given in Figure 5.3, building # 184 was successfully detected as un-collapsed and is represented in green color. In the automatic mode, all the buildings are processed after clicking the 'start' button, located in the automatic segmentation panel (Figure 5.4). Accordingly, the segmentation results and the accuracy assessment statistics are written to an output file with a message, placed on the automatic segmentation panel (Figure 5.4).

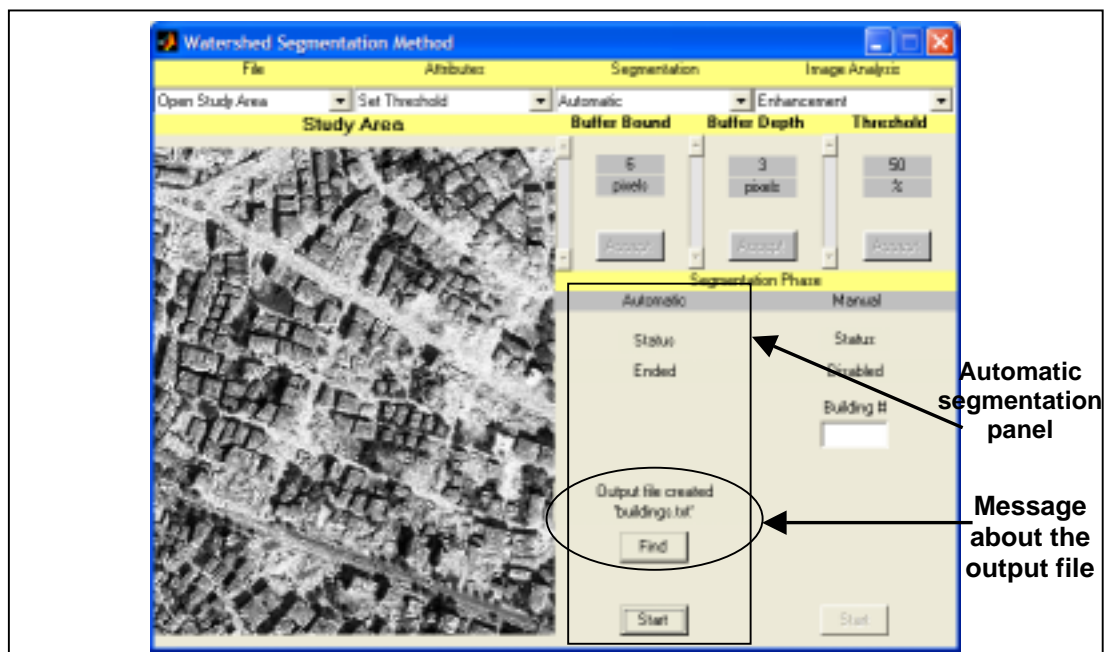


Figure 5.4. View of the automatic segmentation

### 5.3. Building Intensity – Gradient Orientation Component

This component was designed, to implement the second proposed approach for the automated detection of the collapsed buildings from a post-event aerial photo of the damaged region. The source code of this component can be seen in Appendix F.

As in the previous section, the detection procedure starts with the selection of the method in the main window (Figure 5.5). This time, the lower radio button is selected to initiate the building intensity – gradient orientation method.

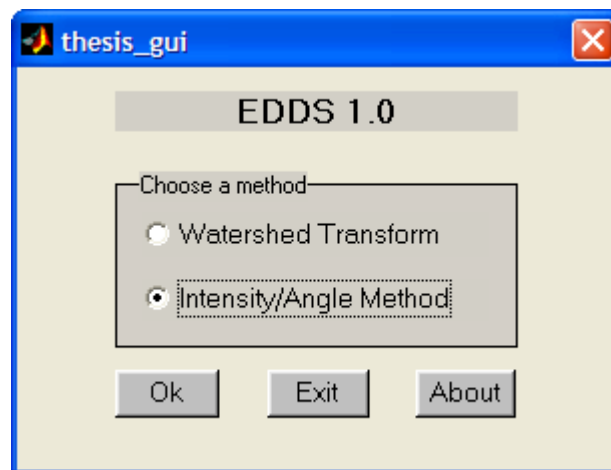


Figure 5.5. Main menu of the damage detection software with second option selected

After selecting the Building Intensity – Gradient Orientation method, a new window is displayed on the screen. This window contains several menu items including file, attributes and detection (Figure 5.6).

- File: As in the watershed segmentation component, this menu contains two options. These are used; (i) to load the study area (aerial photo of the region) and (ii) to terminate the program.

- **Attributes:** The parameters used in the building intensity – gradient orientation approach are available in this menu item. These parameters are; buffer bound, intensity threshold, building ratio and angle threshold (standard deviation threshold). The scroll bars are used to adjust these parameters. The buffer bound parameter gets the pixel values of 0 or 1 that represent the un-buffered and buffered cases of the approach, respectively. On the other hand, the intensity threshold changes between 0 and 255, the building ratio is scaled between 0% and 100% and finally, the angle threshold gets a value between 0 and 100. In the optimum case, if the buffer bound is selected to be 0 then, the other parameters, the intensity threshold, the building ratio and the angle threshold should be chosen as 145, 60% and 17, respectively (Figure 5.6). On the other hand, if the buffer bound is set to 1 then the same parameters should be 141, 60% and 17,31, respectively.

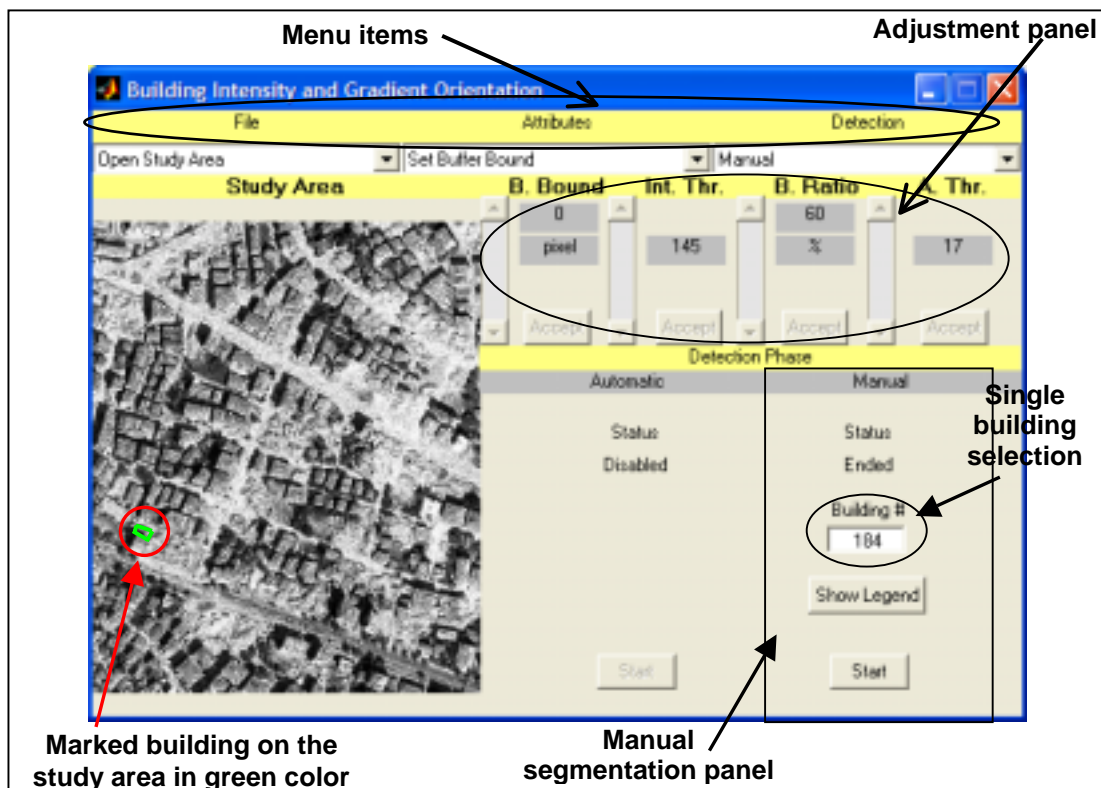


Figure 5.6. General view of the building intensity – gradient orientation interface and the result of the manual detection

- Detection: As in the watershed approach, two types of detection are designed in this approach. These are manual and automatic detections. In both modes, the same logic is used as in the watershed segmentation component. The result of the manual detection is visualized on the aerial photo using four different colors where green represents un-collapsed while red represents the collapsed buildings. On the other hand, blue and yellow colors are used to indicate the omission and commission errors, respectively (Figure 5.6). The results of automatic detection and the statistics of the accuracy assessment are written to a file with a message placed on the automatic detection panel (Figure 5.7).

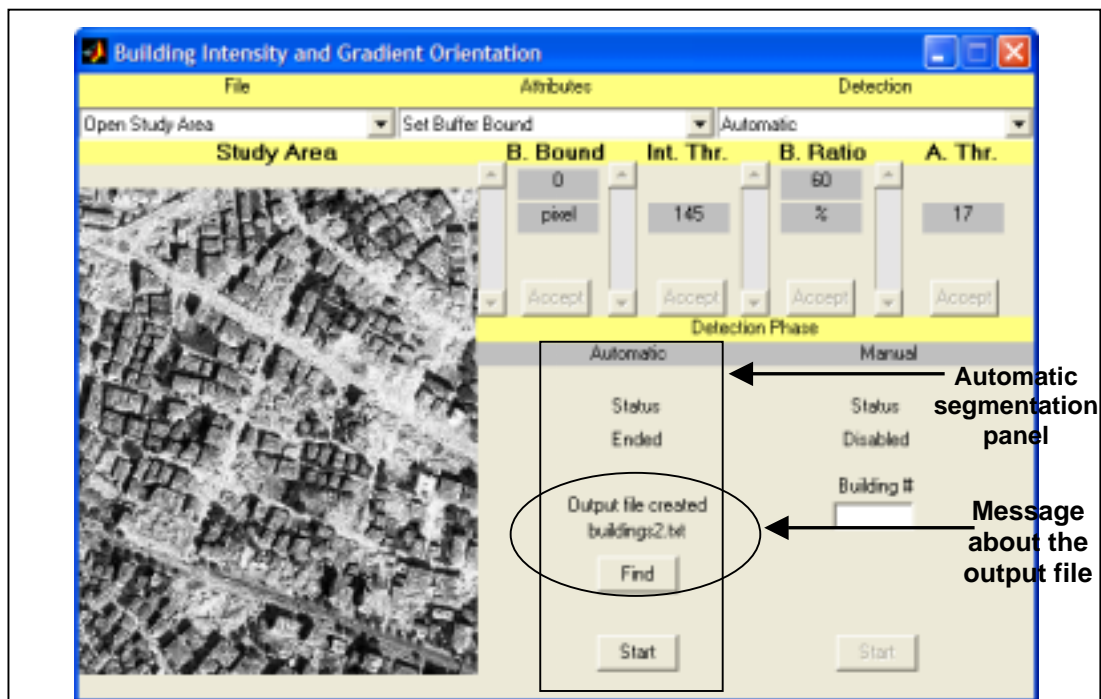


Figure 5.7. View of the automatic detection

#### 5.4. Image Analysis Component

The aim of the image analysis component was to enrich the damage detection software by adding several image processing features. These features include major image enhancement methods and some well-known edge detection algorithms.

The image analysis component is a menu item located within the watershed segmentation component. It contains two options; (i) image enhancement and (ii) edge detection.

- Image Enhancement: In this option, four menu items are available which are file, intensity adjustment, histogram equalization and noise reduction filtering (Figure 5.8).

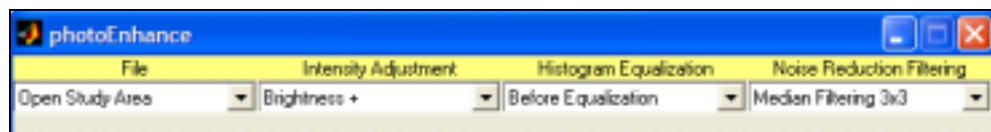


Figure 5.8. Main menu of the image enhancement

The file menu contains the standard options as in the previous components, such as loading the study area and terminating the program. The intensity adjustment offers some modifications on the image. These are simply increasing or decreasing the brightness, contrast and gamma attributes of the image. The effects of these operations, on a small segment of the study area, are exemplified in Figure 5.9. Using the histogram equalization, the intensity histogram of the study area can be equalized. As an output, the modified image can be displayed together with the before and the after histograms (Figure 5.10). In the final menu item, several well-known noise reduction filters

are applied with varying kernel sizes (3x3 and 5x5) to the image. These are; the median, average and adaptive (wiener) filters.

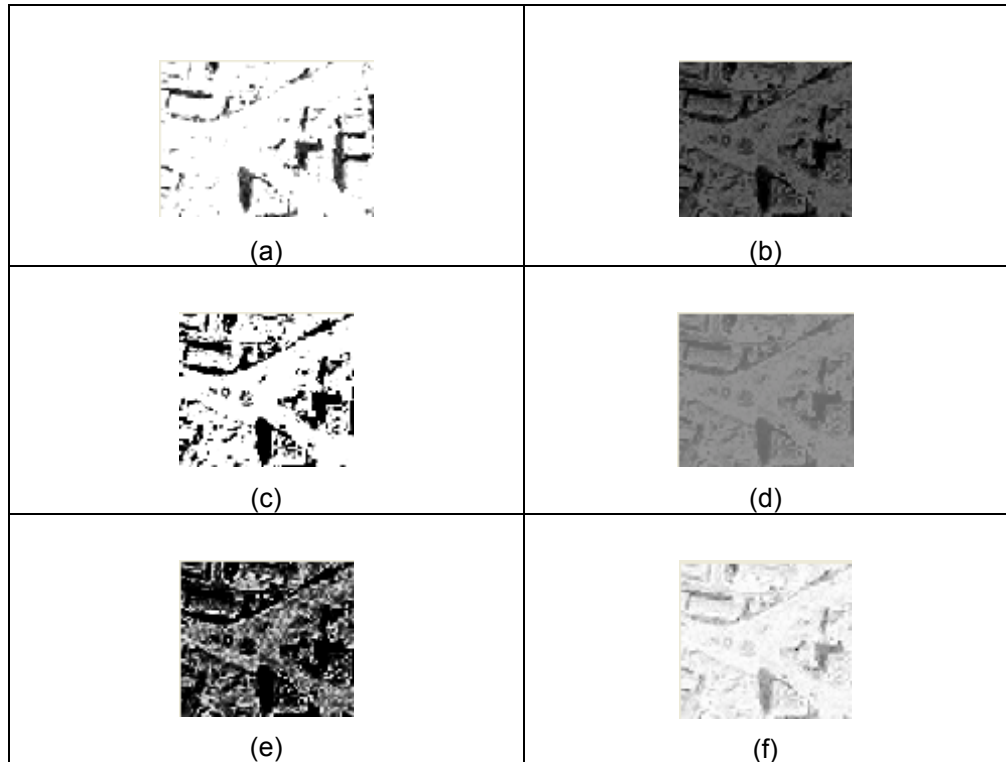


Figure 5.9. (a) High brightness image, (b) low brightness image, (c) high contrast image, (d) low contrast image, (e) high gamma image, (f) low gamma image

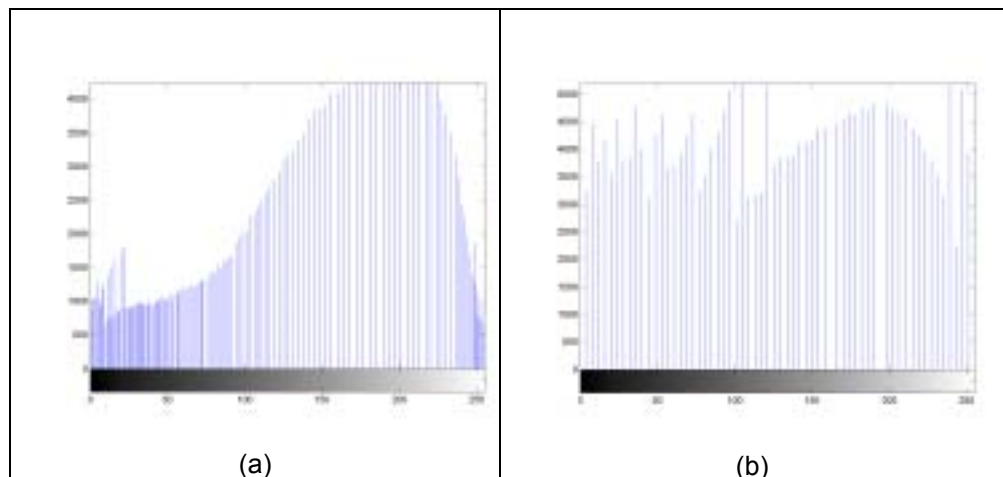


Figure 5.10. The histogram of the (a) original image and (b) equalized image

- Edge Detection: In this menu item, two options are available that are (i) file and (ii) edge detection (Figure 5.11). The content of the file menu is the same as in the previous components. On the other hand, the edge detection is comprised of 5 methods, which are Sobel, Prewitt, Roberts, Laplacian of Gaussian and Canny edge detectors. These methods can be applied to post-event aerial photo of the study area. The resulting images after applying these techniques are illustrated in Figure 5.12.



Figure 5.11. Main menu of the edge detection

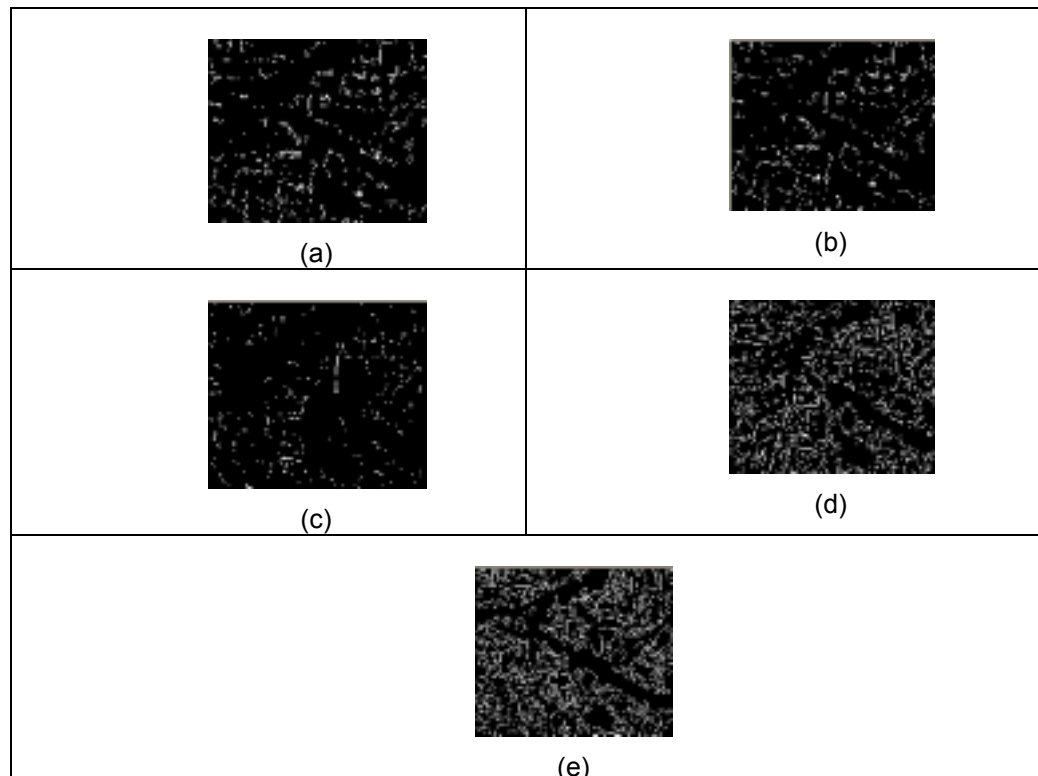


Figure 5.12. Output images after applying (a) Prewitt, (b) Sobel, (c) Roberts, (d) Laplacian of Gaussian and (e) Canny edge filters

## CHAPTER 6

### DISCUSSIONS OF THE RESULTS

In this chapter, two main points are examined. First, the comparison of the proposed (i) watershed segmentation and (ii) building intensity – gradient orientation approaches are carried out in terms of the accuracies of the results they provide and the number of correctly and incorrectly detected buildings. Then, the special cases that make the proposed methods fail are discussed.

#### 6.1. Comparison of the Two Approaches

In the first approach, the building damage detection was achieved using the watershed segmentation algorithm. In the second approach, a composite technique using the intensity of the buildings and the orientation of the gradient was attempted. The second approach was separated into buffered and un-buffered versions. The summary of the results of the developed methods is provided in Table 6.1.

Table 6.1. The comparison of the proposed approaches in terms of overall accuracies

<b>Approach used</b>	<b>Overall Accuracy</b>
<b>Watershed Segmentation</b>	80,63 %
<b>Building Intensity – Gradient Orientation with no buffer</b>	89,44 %
<b>Building Intensity – Gradient Orientation with a pixel wide buffer</b>	90,85 %

As can be seen in the table, all the accuracies are above 80 percent. The highest accuracy (90,85%) was achieved using the buffered version of the building intensity – gradient orientation approach. On the other hand, the lowest accuracy (80,63%) was obtained using the watershed segmentation approach. In addition to overall accuracies, the user’s and producer’s accuracies for collapsed and un-collapsed buildings are also provided in Table 6.2.

Table 6.2. The comparison of the user’s and producer’s accuracies for collapsed and un-collapsed buildings

<b>Approach used</b>	<b>User’s accuracy for collapsed buildings</b>	<b>User’s accuracy for un-collapsed buildings</b>	<b>Producer’s accuracy for collapsed buildings</b>	<b>Producer’s accuracy for un-collapsed buildings</b>
<b>Watershed Segmentation</b>	65,79%	86,06%	63,29%	87,31%
<b>Building Intensity – Gradient Orientation with no buffer</b>	81,01%	92,68%	81,01%	92,68%
<b>Building Intensity – Gradient Orientation with a pixel wide buffer</b>	85,33%	92,82%	81,01%	94,63%

Of the four accuracy indices (user’s accuracy for collapsed, user’s accuracy for un-collapsed, producer’s accuracy for collapsed, producer’s accuracy for un-collapsed), the buffered version of the building intensity – gradient orientation approach provided the highest three accuracies except for the producer’s accuracy for collapsed buildings, which was found to be the same, both in the buffered and un-buffered versions of this approach. This is because of the existence of the equal number of omission errors, which is 15 in buffered and un-buffered cases, shown in Table 6.3. As in the overall accuracies, the watershed segmentation method provided the lowest user’s

and producer’s accuracies. The number of correctly and incorrectly detected buildings by the proposed methods are given in Table 6.3.

Table 6.3. The comparison of the correctly and incorrectly detected buildings with omission and commission errors

<b>Approach used</b>	<b>Number of correctly detected buildings</b>	<b>Number of incorrectly detected buildings</b>	<b>Omission error</b>	<b>Commission error</b>
<b>Watershed Segmentation</b>	229	55	29	26
<b>Building Intensity – Gradient Orientation with no buffer</b>	254	30	15	15
<b>Building Intensity – Gradient Orientation with a one pixel wide buffer</b>	258	26	15	11

As can be seen in Table 6.3, the building intensity – gradient orientation approach was the most successful of all. On the other hand, the watershed segmentation approach was found to be the least successful method. The omission (misclassified collapsed building) and commission (misclassified un-collapsed building) errors were encountered much more in watershed segmentation approach than in the other method. The visual representation of collapsed, un-collapsed and mis-detected buildings for the proposed approaches are presented in the appendices G, H and I.

In the building intensity – gradient orientation approach, small differences were encountered in the results of the buffered and un-buffered versions of the method. For instance, the difference in the overall accuracies was found to be as 1,41%. In the buffered version of this method, the user's and producer's accuracies were slightly better than the un-buffered version. These differences occurred because the buffered version of the method detected four more buildings correctly.

In summary, the results show that both approaches can be accepted successful for detecting the collapsed buildings. However, if compared to each other, the second approach, which was developed based on the intensity and angle information, demonstrates better results than the watershed segmentation approach. It is thought that the difference in the results of the two approaches is due to several special cases about the buildings that negatively affect the detection process and some segmentation errors in the watershed segmentation approach. Moreover, it is clearly seen from the results that the one pixel wide buffer zone improved the accuracy of the second method by providing a better differentiation between collapsed and un-collapsed buildings.

## **6.2. Discussions**

Although the proposed methods were successful for detecting the damaged buildings, in several cases, incorrect labeling of the buildings was observed. This may be due to the shortcomings of the methods and several special cases. These cases and limitations were examined in detail and examples were provided for each case.

The limitations and several special cases encountered during the study are listed below with the example aerial photos:

1. The shadow of the neighboring object casts on an un-collapsed building: This case is illustrated in Figure 6.1

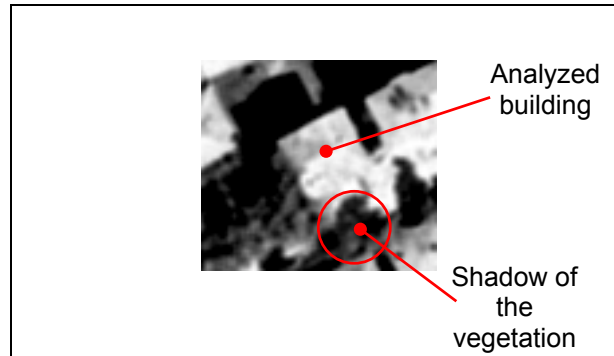


Figure 6.1. An example for the limitation # 1

This case is only encountered in the watershed segmentation approach. In this case, the shadow of the vegetation casts on an un-collapsed building. For this reason, the building is labeled as collapsed due to insufficient building pixels.

2. The shadow of the neighboring object casts on a collapsed building: This case is exemplified in Figure 6.2

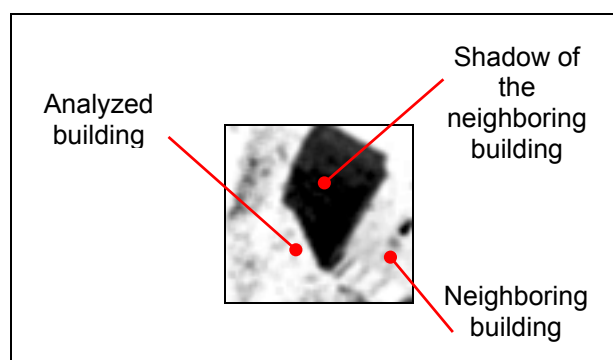


Figure 6.2. An example for the limitation # 2

This special case was faced in both approaches. In watershed segmentation approach, the shadow pixels of the analyzed building increases due to the shadow of the neighboring building. Therefore, the collapsed building is labeled un-collapsed. On the other hand, in the building intensity – gradient orientation approach, the intensity of the building is reduced due to the shadow of the neighboring building. Thus, like in the watershed segmentation method, the collapsed building is marked as un-collapsed.

3. The shadow of an un-collapsed building is obscured by a neighboring building: An example of this case is shown in Figure 6.3.

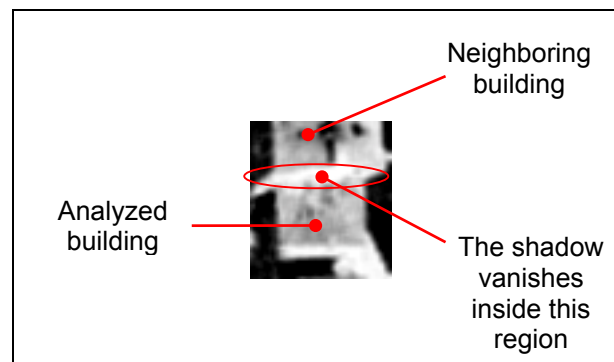


Figure 6.3. An example for the limitation # 3

This case was observed in the watershed segmentation approach only. The neighboring building obscures the shadow region of an un-collapsed building. As a consequence, the shadow pixels of the analyzed building are reduced and the building is mis-detected as collapsed.

4. The occurrence of low contrast between a building and the shadows: This case is shown in Figure 6.4.

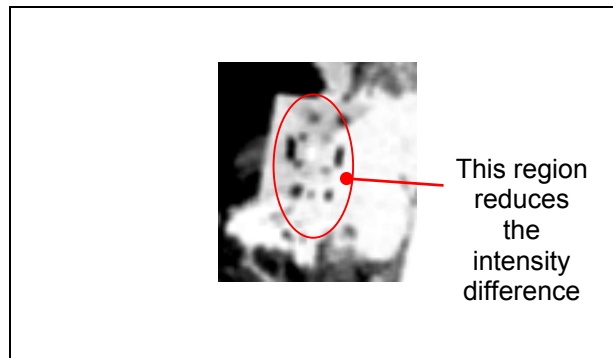


Figure 6.4. An example for the limitation # 4

This anomaly was met in both approaches. In the watershed segmentation approach, the building pixels are diminished inside the building polygon due to low intensity spots. Therefore, the building being analyzed is incorrectly labeled collapsed instead of un-collapsed. In the building intensity – gradient orientation approach, a heterogeneous texture may occur due to the chimneys and some other objects located on the roof of the building, shown in the above figure. This texture increases the standard deviation of the angle histogram of the gradient image and therefore, the standard deviation exceeds the optimum threshold value. Thus, the un-collapsed building is wrongly labeled collapsed.

5. A collapsed building casts shadow to some extent : This limitation is illustrated in Figure 6.5.

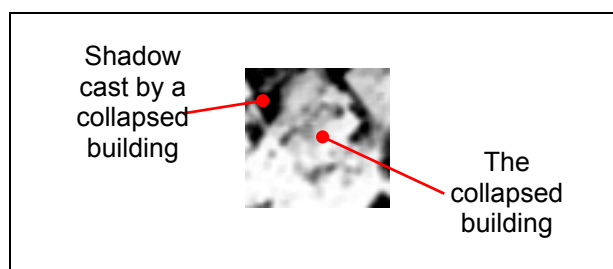


Figure 6.5. An example for the limitation # 5

This case is encountered in both approaches. In the watershed segmentation approach, the unexpected cast shadows around the building polygon increases the shadow pixels. As a consequence, the collapsed building is labeled un-collapsed due to this case. In the second approach, the building intensity is reduced due to the shadow region cast by the collapsed building. This causes the incorrect labeling of a collapsed building as un-collapsed.

6. An error occurs in segmentation due to the location of the markers: This case is illustrated in Figure 6.6

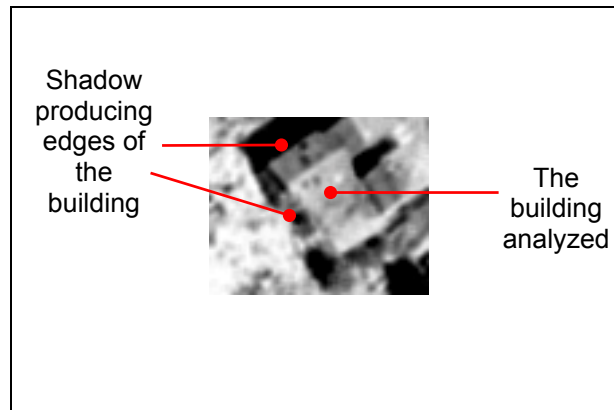


Figure 6.6. An example for the limitation # 6

This kind of error occurs only in the watershed segmentation approach. If one of the shadow casting edges of the building being analyzed does not produce enough shadow, the initial points (markers) for the shadow region may not be selected properly. Therefore, due to this reason, a false output is created and an un-collapsed building may be labeled collapsed.

After examining the mentioned cases above, the distribution of the mis-detected buildings with respect to these cases are given, for each method in Table 6.4.

Table 6.4. The distribution of the mis-detected buildings according to six cases

<b>Approach used</b>	<b>Case #1</b>	<b>Case #2</b>	<b>Case #3</b>	<b>Case #4</b>	<b>Case #5</b>	<b>Case #6</b>	<b>Total Mis-detected buildings</b>
<b>Watershed Segmentation</b>	2	3	8	11	26	5	55
<b>Building Intensity – Gradient Orientation (with no buffer)</b>	0	6	0	15	9	0	30
<b>Building Intensity – Gradient Orientation (with a pixel wide buffer)</b>	0	6	0	11	9	0	26

It is evident from the above table that most of the mis-detections are arisen from two shortcomings. The first limitation comes with the unexpected shadows cast by the collapsed buildings that cause to fail the detection process. The second one is the occurrence of low contrast between the buildings and their cast shadows.

In addition to the listed limitations, the proposed approaches may not be successful in the following cases:

- If the sunrays come towards the ground at 90° angle, the detection of the shadows of the buildings would be more difficult because the cast shadows would be thin.
- Those buildings small in size and/or low in height may not produce enough shadow. Therefore, the detection of these buildings may be difficult.

- The non-rectangular shape buildings (circular, elliptical or polygonal more than four edges) may not be detected properly due to the mis-identification of the shadow edges.
- The buildings having a very light roof in color (almost white) may not be detected correctly by the building intensity analysis.

## CHAPTER 7

### CONCLUSIONS AND RECOMMENDATIONS

In this chapter, the conclusions of the conducted research are described together with the recommendations related to further studies. This chapter is composed of three sections. In the first two sections, the conclusions of the watershed segmentation and the building intensity – gradient orientation approaches are provided, respectively. Then, in the last section, the recommendations are presented.

#### 7.1. Conclusions of Watershed Segmentation Approach

In this part, an approach for detecting the earthquake-damaged buildings through shadow analysis of the watershed segmented post-event aerial imagery is presented. The approach was implemented in an urban area of the city of Golcuk. A total of 284 buildings were analyzed to measure their conditions. Of the 79 collapsed buildings, 50 were detected correctly providing a producer's accuracy of 63.29% and a user's accuracy of 65.79%. On the other hand, of the 205 un-collapsed buildings, 179 were labeled correctly providing a producer's accuracy of 87.31% and a user's accuracy of 86.06%. The overall accuracy was computed as 80.63%.

It was found that determining the optimum threshold for separating the damaged buildings from non-damaged is important. In the present case, the optimum threshold was computed as 50% by using various accuracy indices. This threshold value is valid for this study only, and should not be considered global.

In this approach, the integration of the raster data (aerial photo of the region struck by the earthquake) with the GIS data (vector building boundaries) was found to be very helpful. By doing this, it was purely concentrated on building polygons and the false alarm areas, such as vegetation and roads, were not taken into account. Thus, the overall accuracy was improved.

In addition, development of a system that provides the automated detection of the collapsed buildings had many advantages. The first benefit was the reduction of the processing speed. The other one was the provision of a user-friendly environment. Moreover, as a by-product, generation of the visual and textual outputs enhanced the results of the analyses. Finally, it was concluded that the results of the detection of collapsed buildings using watershed segmentation are found to be fairly encouraging.

## **7.2. Conclusions of Building Intensity – Gradient Orientation Approach**

In this section, an alternative approach, building intensity – gradient orientation, based on building intensity information together with the angle information of the gradient image is explained. This approach was also implemented in the same area of the city of Golcuk, so as to compare the results of the two approaches. In the analysis of the buildings, two different experiments were carried out. In the first experiment, 284 buildings were analyzed without using a buffer area. Of the 79 collapsed buildings, 64 were detected correctly providing the producer's and user's accuracies of 81,01%. On the other hand, of the 205 un-collapsed buildings, 190 were labeled correctly providing the producer's and user's accuracies of 92.68%. The overall accuracy was computed to be 89.44%. In the second experiment, all the buildings were analyzed by using a one-pixel wide buffer area around the building polygons. This time, of the 79 collapsed buildings, 64 were detected correctly providing a producer's accuracy of 81.01% and a user's accuracy of

85.33%. On the other hand, of the 205 un-collapsed buildings, 194 were labeled correctly providing a producer's accuracy of 94.63% and a user's accuracy of 92.82%. The overall accuracy was computed to be 90.85%. As a result of building intensity – gradient orientation approach, when a buffer was used, the accuracy of the result increased.

In this approach, three different threshold levels (intensity threshold, building ratio and standard deviation threshold) were used and found to be vital in discriminating the collapsed buildings from the un-collapsed. In the present case, the optimum threshold values were computed as (141, 60%, 17.31) and (145, 60%, 17) for the buffered and un-buffered cases, respectively. However, these values were obtained for this study and may not be applied to different study areas.

A system was also developed in order to provide the automated detection of the collapsed buildings. Using this system, the comparison of the results of the two proposed approaches were effectively carried out.

Finally, the integration of raster data and GIS data was efficiently performed and found to be very functional in this approach. The results of the building intensity – gradient orientation approach were regarded as quite promising due to its high accuracy.

### **7.3. Recommendations**

The watershed segmentation approach has several shortcomings to be improved in the future. The selection of the initial markers is one problem. The buffer zones that are defined by the user can be expanded or shrunk to find a better agreement between the shadow pixels (generated by the algorithm) and the actual shadow pixels.

The building intensity – gradient orientation approach has also some limitations such as the size of the buffer and type of the filter used for smoothing the building image patches. The optimum size for the building buffer should be determined to produce better results. In addition, the use of an adaptive filter instead of a standard Gaussian filter may yield better results.

The proposed approaches can be applied on high-resolution satellite images or aerial images higher than one-meter spatial resolution. Working with a high-resolution data may eliminate some of the shortcomings mentioned in chapter 6.

The developed software can be improved by adding several processing modules that perform an automatic detection of the building boundaries. By doing this, the capabilities and the speed of the system may be enhanced by eliminating the external use of GIS data.

## REFERENCES

1. Alexander, D., (1993), Natural Disasters, **United** Kingdom: USL Press.
2. Beucher, S. and Meyer, F., (1992), The morphological approach of segmentation: the watershed transformation. In: Mathematical Morphology in Image Processing, E. Dougherty, Ed., chapter 12, pp. 433–481. Marcel Dekker, New York.
3. EDM, (2000), Report on the Kocaeli, TURKEY earthquake of August 17, 1999, EDM Technical Report No.6, Earthquake Disaster Mitigation Center, The Institute of Physical and Chemical Research.
4. Estrada, M., Kohiyama, M., Matsuoka, M. and Yamazaki, F., (2001), Detection of Damage Due to the 2001 El Salvador Earthquake Using Landsat Images, Proceedings of the 22nd Asian Conference on Remote Sensing, Singapore, Vol.2, pp.1372-1377.
5. Fung., T. and LeDrew, E., (1988), The Determination of Optimal Threshold Levels for Change Detection Using Various Accuracy Indices, Photogrammetric Engineering and Remote Sensing, Vol.54, No.10, pp.1449-1454.
6. Gamba, P. and Casciati, F., (1998), GIS and Image Understanding for Near-Real-Time Earthquake Damage Assessment, Photogrammetric Engineering and Remote Sensing, Vol.64, No.10, pp.987-994.
7. Hasegawa, H., Aoki, H., Yamazaki, F. and Sekimoto, I., (1999), Attempt for Automated Detection of Damaged Buildings Using Aerial HDTV Images, Proceedings of the 20th Asian Conference on Remote Sensing, Vol.1, pp.97-102.
8. Huertas, A. and Nevatia, R., (1988), Detecting Buildings in Aerial Images, Computer Vision, Graphics, and Image Processing, Vol.41, pp.131-152.

9. Irvin, R.B., and McKeown, D.M., (1989), Methods for Exploiting the Relationship Between Buildings and Their Shadows in Aerial Imagery, IEEE Transactions On Systems, Man, and Cybernetics, Vol.19, No.6, pp.1564-1575.
10. Ishii, M., Goto, T., Sugiyama, T., Saji, H. and Abe, K.,(2001), Detection of Earthquake Damaged Areas from Aerial Photographs by Using Color and Edge Information, IPSJ SIGNotes Computer Vision and Image Media, No.127 – 026.
11. MATLAB 6.5.0 manual, (2002), Learning Matlab, Getting Started – Introduction to Matlab.
12. Mitomi, H., Yamazaki, F. and Matsuoka, M., (2000), Automated Detection of Building Damage due to Recent Earthquakes Using Aerial Television Images, 21<sup>st</sup> Asian Conference on Remote Sensing, Vol.1, pp.401-406.
13. Montoya, L., (2002), Urban Disaster Management A Case Study of Earthquake Risk Assessment in Cartago, Costa Rica. PhD Thesis submitted to Utrecht University, Netherlands.
14. Ozisik, D., (2004), Post-earthquake Damage Assessment Using Satellite and Aerial Video Imagery, Master Thesis submitted to the International Institute for Geo-information Science and Earth Observation, Netherlands.
15. San, B.T., (2002), Detecting Earthquake Induced Changes From Space and Aerial Images, Master Thesis submitted to the Graduate School of Natural and Applied Sciences, Middle East Technical University, Turkey.
16. Shafarenko, L., Petrou, M. and Kittler, J., (1997), Automatic Watershed Segmentation of Randomly Textured Color Images. IEEE Trans. Image Processing, 6(11), pp. 1530-1544.
17. Sonka, M., Hlavac, V. and Boyle, R., (1998), Image Processing, Analysis, and Machine Vision, 2nd Edition, Brooks Cole, USA, pp. 186-188.

18. Story, M. and Congalton, R.G., (1986), Accuracy Assessment: A User's Perspective, Photogrammetric Engineering and Remote Sensing, Vol.52, No.3, pp.397-399.
19. Turker, M. and Cetinkaya, B., (in press), Automatic detection of earthquake damaged buildings using DEMs created from pre- and post-earthquake stereo aerial photographs. International Journal of Remote Sensing.
20. Turker, M. and San, B.T., (2003), SPOT HRV data analysis for detecting earthquake-induced changes in Izmit, Turkey, International Journal of Remote Sensing, Vol.24, No.12, pp.2439-2450.
21. Turker, M. and San, B.T., (in press), Detection of collapsed buildings caused by the 1999 Izmit, Turkey earthquake through digital analysis of post-event aerial photographs. International Journal of Remote Sensing.
22. Vincent, L. and Soille, P., (1991), Watersheds in digital spaces: an efficient algorithm based on immersion simulations. IEEE Transactions on Pattern Analysis and Machine Intelligence, 13(6), pp. 583-598.
23. Yamazaki, F., (2001), Applications of Remote Sensing and GIS for Damage Assessment. Bangkok: International Center for Urban Safety.
24. Yusuf, Y., Matsuoka, M. and Yamazaki, F., (2001), Damage Detection from Landsat-7 Satellite Images for the 2001 Gujarat, India Earthquake, Proceedings of the 22nd Asian Conference on Remote Sensing, Singapore, Vol.1, pp.300-305.
25. Yanamura, Y. and Saji, H., (2003), Automatic Registration of Aerial Image and Digital Map for Detection of Earthquake Damaged Areas, Proceedings of the VII<sup>th</sup> Digital Image Computing: Techniques and Applications, 117-126.

## ONLINE REFERENCES

1. Chiroiu, L. and Andre, G., (2001), Damage Assessment Using High Resolution Satellite Imagery: Application to 2001 Bhuj, India, Earthquake. Retrieved 20 July 2004, from the World Wide Web: <http://www.riskworld.com/Nreports/2001/Bhuj,India,earthquake2001.PDF>
2. Erdik, M., (2003), Report on 1999 Kocaeli and Duzce (Turkey) Earthquakes. Retrieved 12 July 2004, from the World Wide Web: <http://www.koeri.boun.edu.tr/depremmuh/Kocaelireport.pdf>
3. Ham, D., (1998), Aerial Photography and Videography Standards: Applications for Stream Inventory and Assessment. Retrieved: 10 July 2004, from the World Wide Web: <http://srmwww.gov.bc.ca/risc/pubs/aquatic/aerialvideo/aerialvid-04.htm>
4. Huyck, C., Mansori, B., Eguchi, R., Houshmand, B., Castner, L. and Shinozuka, M., (2003), Earthquake Damage Detection Algorithms Using Optical and ERS-Sar Satellite Data – Application to the August 17, 1999 Marmara, Turkey Earthquake. Retrieved 10 July 2004, from the World Wide Web: <http://imagecatinc.com/reportspubs/00105.pdf>
5. Lecture Notes on Image Processing Algorithms Course, (2002), Graduate School of Informatics, Middle East Technical University, Turkey. Retrieved 3 June 2004, from the World Wide Web: <http://online.metu.edu.tr/online/courses/is566/lectures/lectures/6/3/index.html>
6. Mitomi, H., Yamazaki, F., Matsuoka, M., Taniguchi, H. and Ogawa, Y., (2003), Determination of Areas with Building Damage due to the Kobe Earthquake Using Airborne MSS Images. Retrieved 30 June 2004, from the World Wide Web: [http://www.edm.bosai.go.jp/team2/matsu/others/igarss02\\_hm.pdf](http://www.edm.bosai.go.jp/team2/matsu/others/igarss02_hm.pdf)
7. Van Westen, C. and Hofstee, P., (2001), The Role of Remote Sensing and GIS in Risk Mapping and Damage Assessment for Disasters in Urban Areas. Retrieved 10 July 2004, from the World Wide Web: <http://www.dkkv.org/forum/2001/Datei61.pdf>

**APPENDIX A: ERROR MATRICES FOR THE VARYING THRESHOLD  
VALUES BETWEEN 20% AND 80%**

Table A.1. Error matrix for the threshold level of 20%

	Reference		
	Collapsed	Un-collapsed	Total
Collapsed	3	1	4
Un-collapsed	76	204	280
Total	79	205	284

Table A.2. Error matrix for the threshold level of 30%

	Reference		
	Collapsed	Un-collapsed	Total
Collapsed	15	4	19
Un-collapsed	64	201	265
Total	79	205	284

Table A.3. Error matrix for the threshold level of 40%

	Reference		
	Collapsed	Un-collapsed	Total
Collapsed	30	15	45
Un-collapsed	49	190	239
Total	79	205	284

Table A.4. Error matrix for the threshold level of 50%

	Reference		
	Collapsed	Un-collapsed	Total
Collapsed	50	26	76
Un-collapsed	29	179	208
Total	79	205	284

Table A.5. Error matrix for the threshold level of 60%

	Reference		
	Collapsed	Un-collapsed	Total
Collapsed	62	55	117
Un-collapsed	17	150	167
Total	79	205	284

Table A.6. Error matrix for the threshold level of 70%

	Reference		
	Collapsed	Un-collapsed	Total
Collapsed	71	94	165
Un-collapsed	8	111	119
Total	79	205	284

Table A.7. Error matrix for the threshold level of 80%

	Reference		
	Collapsed	Un-collapsed	Total
Collapsed	76	160	236
Un-collapsed	3	45	48
Total	79	205	284

## APPENDIX B: CALCULATIONS OF THE ACCURACY INDICES FOR THE THRESHOLD LEVELS BETWEEN 20% and 80%

Calculation of the accuracy indices for the threshold level of 20% using the corresponding error matrix:

➤ Overall Accuracy =  $(3 + 204) / 284 * 100 = 72,89\%$

➤ Overall Kappa =  $(a_{\text{overall}} - a_{\text{observed}}) / (1 - a_{\text{observed}})$ ,

$$a_{\text{observed}} = \frac{(79 * 4) + (280 * 205)}{(4 * 79) + (280 * 205) + (4 * 205) + (79 * 280)} = 0.0471$$

➤ User's accuracy for collapsed buildings =  $3 / 4 * 100 = 75\%$

➤ User's accuracy for un-collapsed buildings =  $204 / 280 * 100 = 72,86\%$

➤ Average user's accuracy =  $(75 + 72,86) / 2 = 73,93\%$

➤ Producer's accuracy for collapsed buildings =  $3 / 79 * 100 = 3,80\%$

➤ Producer's accuracy for un-collapsed buildings =  $204 / 205 * 100 = 99,51\%$

➤ Average producer's accuracy =  $(3,80 + 99,51) / 2 = 51,66\%$

➤ Combined user's accuracy =  $(\text{Overall accuracy} + \text{Average user's accuracy}) / 2 = (72,89 + 73,93) / 2 = 73,41\%$

➤ Combined producer's accuracy =  $(\text{Overall accuracy} + \text{Average producer's accuracy}) / 2 = (72,89 + 51,66) / 2 = 62,28\%$

Calculation of the accuracy indices for the threshold level of 30% using the corresponding error matrix:

➤ Overall Accuracy =  $(15 + 201) / 284 * 100 = \mathbf{76,06\%}$

➤ Overall Kappa =  $(a_{\text{overall}} - a_{\text{observed}}) / (1 - a_{\text{observed}})$ ,

$$a_{\text{observed}} = \frac{(79 * 19) + (265 * 205)}{(19 * 79) + (19 * 205) + (79 * 265) + (205 * 265)} = \mathbf{0.2224}$$

➤ User's accuracy for collapsed buildings =  $15 / 19 * 100 = \mathbf{78,95\%}$

➤ User's accuracy for un-collapsed buildings =  $201 / 265 * 100 = \mathbf{75,85\%}$

➤ Average user's accuracy =  $(78,95 + 75,85) / 2 = \mathbf{77,40\%}$

➤ Producer's accuracy for collapsed buildings =  $15 / 79 * 100 = \mathbf{18,99\%}$

➤ Producer's accuracy for un-collapsed buildings =  $201 / 205 * 100 = \mathbf{98,05\%}$

➤ Average producer's accuracy =  $(18,99 + 98,05) / 2 = \mathbf{58,52\%}$

➤ Combined user's accuracy =  $(\text{Overall accuracy} + \text{Average user's accuracy}) / 2 = (76,06 + 77,40) / 2 = \mathbf{76,73\%}$

➤ Combined producer's accuracy =  $(\text{Overall accuracy} + \text{Average producer's accuracy}) / 2 = (76,06 + 58,52) / 2 = \mathbf{67,29\%}$

Calculation of the accuracy indices for the threshold level of 40% using the corresponding error matrix:

➤ Overall Accuracy =  $(30 + 190) / 284 * 100 = 77,46\%$

➤ Overall Kappa =  $(a_{\text{overall}} - a_{\text{observed}}) / (1 - a_{\text{observed}})$ ,

$$a_{\text{observed}} = \frac{(79 * 45) + (239 * 205)}{(45 * 79) + (79 * 239) + (239 * 205) + (45 * 205)} = 0.3532$$

➤ User's accuracy for collapsed buildings =  $30 / 45 * 100 = 66,67\%$

➤ User's accuracy for un-collapsed buildings =  $190 / 239 * 100 = 79,50\%$

➤ Average user's accuracy =  $(66,67 + 79,50) / 2 = 73,09\%$

➤ Producer's accuracy for collapsed buildings =  $30 / 79 * 100 = 37,97\%$

➤ Producer's accuracy for un-collapsed buildings =  $190 / 205 * 100 = 92,68\%$

➤ Average producer's accuracy =  $(37,97 + 92,68) / 2 = 65,33\%$

➤ Combined user's accuracy =  $(\text{Overall accuracy} + \text{Average user's accuracy}) / 2 = (77,46 + 73,09) / 2 = 75,28\%$

➤ Combined producer's accuracy =  $(\text{Overall accuracy} + \text{Average producer's accuracy}) / 2 = (77,46 + 65,33) / 2 = 71,40\%$

Calculation of the accuracy indices for the threshold level of 60% using the corresponding error matrix:

➤ Overall Accuracy =  $(62 + 150) / 284 * 100 = 74,65\%$

➤ Overall Kappa =  $(a_{\text{overall}} - a_{\text{observed}}) / (1 - a_{\text{observed}})$ ,

$$a_{\text{observed}} = \frac{(79 * 117) + (167 * 205)}{(117 * 79) + (117 * 205) + (79 * 167) + (205 * 167)} = 0.4501$$

➤ User's accuracy for collapsed buildings =  $62 / 117 * 100 = 52,99\%$

➤ User's accuracy for un-collapsed buildings =  $150 / 167 * 100 = 89,82\%$

➤ Average user's accuracy =  $(52,99 + 89,82) / 2 = 71,41\%$

➤ Producer's accuracy for collapsed buildings =  $62 / 79 * 100 = 78,48\%$

➤ Producer's accuracy for un-collapsed buildings =  $150 / 205 * 100 = 73,17\%$

➤ Average producer's accuracy =  $(78,48 + 73,17) / 2 = 75,83\%$

➤ Combined user's accuracy =  $(\text{Overall accuracy} + \text{Average user's accuracy}) / 2 = (74,65 + 71,41) / 2 = 73,03\%$

➤ Combined producer's accuracy =  $(\text{Overall accuracy} + \text{Average producer's accuracy}) / 2 = (74,65 + 75,83) / 2 = 75,24\%$

Calculation of the accuracy indices for the threshold level of 70% using the corresponding error matrix:

➤ Overall Accuracy =  $(71 + 111) / 284 * 100 = \mathbf{64,08\%}$

➤ Overall Kappa =  $(a_{\text{overall}} - a_{\text{observed}}) / (1 - a_{\text{observed}})$ ,

$$a_{\text{observed}} = \frac{(79 * 165) + (119 * 205)}{(165 * 79) + (165 * 205) + (79 * 119) + (205 * 119)} = \mathbf{0.3298}$$

➤ User's accuracy for collapsed buildings =  $71 / 165 * 100 = \mathbf{43,03\%}$

➤ User's accuracy for un-collapsed buildings =  $111 / 119 * 100 = \mathbf{93,28\%}$

➤ Average user's accuracy =  $(43,03 + 93,28) / 2 = \mathbf{68,15\%}$

➤ Producer's accuracy for collapsed buildings =  $71 / 79 * 100 = \mathbf{89,87\%}$

➤ Producer's accuracy for un-collapsed buildings =  $111 / 205 * 100 = \mathbf{54,15\%}$

➤ Average producer's accuracy =  $(89,87 + 54,15) / 2 = \mathbf{72,01\%}$

➤ Combined user's accuracy =  $(\text{Overall accuracy} + \text{Average user's accuracy}) / 2 = (64,08 + 68,15) / 2 = \mathbf{66,12\%}$

➤ Combined producer's accuracy =  $(\text{Overall accuracy} + \text{Average producer's accuracy}) / 2 = (64,08 + 72,01) / 2 = \mathbf{68,05\%}$

Calculation of the accuracy indices for the threshold level of 80% using the corresponding error matrix:

➤ Overall Accuracy =  $(76 + 45) / 284 * 100 = \mathbf{42,61\%}$

➤ Overall Kappa =  $(a_{\text{overall}} - a_{\text{observed}}) / (1 - a_{\text{observed}})$ ,

$$a_{\text{observed}} = \frac{(79 * 236) + (48 * 205)}{(236 * 79) + (236 * 205) + (79 * 48) + (205 * 48)} = \mathbf{0.1128}$$

➤ User's accuracy for collapsed buildings =  $76 / 236 * 100 = \mathbf{32,20\%}$

➤ User's accuracy for un-collapsed buildings =  $45 / 48 * 100 = \mathbf{93,75\%}$

➤ Average user's accuracy =  $(32,20 + 93,75) / 2 = \mathbf{62,98\%}$

➤ Producer's accuracy for collapsed buildings =  $76 / 79 * 100 = \mathbf{96,20\%}$

➤ Producer's accuracy for un-collapsed buildings =  $45 / 205 * 100 = \mathbf{21,95\%}$

➤ Average producer's accuracy =  $(96,20 + 21,95) / 2 = \mathbf{59,08\%}$

➤ Combined user's accuracy =  $(\text{Overall accuracy} + \text{Average user's accuracy}) / 2 = (42,61 + 62,98) / 2 = \mathbf{52,80\%}$

➤ Combined producer's accuracy =  $(\text{Overall accuracy} + \text{Average producer's accuracy}) / 2 = (42,61 + 59,08) / 2 = \mathbf{50,85\%}$

## APPENDIX C: CALCULATION OF OPTIMUM BUILDING INTENSITY THRESHOLD LEVEL

Normal Distribution Curve Equation:

$$y = f(x | \mu, \sigma) = \frac{1}{\sigma (2\pi)^{1/2}} e^{-\frac{(x - \mu)^2}{2\sigma^2}} \quad -\infty < x < \infty$$

$f_{col}(x)$ : Normal distribution curve function for collapsed buildings

$f_{uncol}(x)$ : Normal distribution curve for un-collapsed buildings

$\mu_{col}$ : The mean value of the collapsed buildings = (171,26)

$\sigma_{col}$ : The standard deviation of the collapsed buildings = (25,17)

$\mu_{uncol}$ : The mean value of the un-collapsed buildings = (120,61)

$\sigma_{uncol}$ : The standard deviation of the un-collapsed buildings = (20,63)

In order to find the intersection of the two functions,  $f_{col}(x) = f_{uncol}(x)$  should be satisfied as follows:

$$f_{col}(x) = \frac{1}{\sigma_{col} (2\pi)^{1/2}} e^{-\frac{(x - \mu_{col})^2}{2\sigma_{col}^2}} = f_{uncol}(x) = \frac{1}{\sigma_{uncol} (2\pi)^{1/2}} e^{-\frac{(x - \mu_{uncol})^2}{2\sigma_{uncol}^2}}$$

$$\frac{1}{25,17 (6,28)^{1/2}} e^{-\frac{(x - 171,26)^2}{2(25,17)^2}} = \frac{1}{20,63 (6,28)^{1/2}} e^{-\frac{(x - 120,61)^2}{2(20,63)^2}}$$

$$\frac{25,17}{20,63} = e^{-\frac{(x - 171,26)^2}{1267,06}} \bigg/ e^{-\frac{(x - 120,61)^2}{851,19}}$$

$$\ln \frac{25,17}{20,63} = \ln e^{\frac{-(x - 171.26)^2}{1267.06} + \frac{(x - 120.61)^2}{851.19}}$$

$$0.19885 = x^2 \left( \frac{1}{851.19} - \frac{1}{1267.06} \right) - 0.0131x - 6.058$$

$$0.000385x^2 - 0.0127x - 6.25685 = 0$$

Positive x is found as 145, which is the optimum intensity threshold.

**APPENDIX D: CALCULATION OF OPTIMUM BUILDING INTENSITY  
THRESHOLD LEVEL WITH 1 PIXEL WIDE BUFFER  
REGION**

Normal Distribution Curve Equation:

$$y = f(x | \mu, \sigma) = \frac{1}{\sigma(2\pi)^{1/2}} e^{-\frac{(x - \mu)^2}{2\sigma^2}} \quad -\infty < x < \infty$$

$f_{col}(x)$ : Normal distribution curve function for collapsed buildings

$f_{uncol}(x)$ : Normal distribution curve for un-collapsed buildings

$\mu_{col}$ : The mean value of the collapsed buildings = (170,52)

$\sigma_{col}$ : The standard deviation of the collapsed buildings = (24,67)

$\mu_{uncol}$ : The mean value of the un-collapsed buildings = (114,34)

$\sigma_{uncol}$ : The standard deviation of the un-collapsed buildings = (20,96)

In order to find the intersection of the two functions,  $f_{col}(x) = f_{uncol}(x)$  should be satisfied as follows:

$$f_{col}(x) = \frac{1}{\sigma_{col}(2\pi)^{1/2}} e^{-\frac{(x - \mu_{col})^2}{2\sigma_{col}^2}} = f_{uncol}(x) = \frac{1}{\sigma_{uncol}(2\pi)^{1/2}} e^{-\frac{(x - \mu_{uncol})^2}{2\sigma_{uncol}^2}}$$

$$\frac{\cancel{1}}{\cancel{20.96} (6.28)^{1/2}} e^{-\frac{(x - 114.34)^2}{2(20.96)^2}} = \frac{\cancel{1}}{\cancel{24.67} (6.28)^{1/2}} e^{-\frac{(x - 170.52)^2}{2(24.67)^2}}$$

$$\frac{24,67}{20,96} = e^{-\frac{(x - 170.52)^2}{1217.22}} \bigg/ e^{-\frac{(x - 114.34)^2}{878.64}}$$

$$\ln \frac{25,17}{20,63} = \ln e^{\frac{-(x - 170.52)^2}{1217.22} + \frac{(x - 114.34)^2}{878.64}}$$

$$0.163 = x^2 \left( \frac{1}{878.64} - \frac{1}{1217.22} \right) - 0.02x - 9.17$$

$$0.000316x^2 - 0.0205x - 9.17 = 0$$

Positive x is found as 141, which is the optimum intensity threshold.



```

datum
end
for i = 1 : build_size(b)
XArray(b,i) = s(b,i).X;
YArray(b,i) = s(b,i).Y;
XEdgeIndex(b,i) = s(b,i).edgeIndex;
end
min_x = min(XArray(b,1:build_size(b)));
max_x = max(XArray(b,1:build_size(b)));
min_y = min(YArray(b,1:build_size(b)));
max_y = max(YArray(b,1:build_size(b)));
temp = im(min_y-bufferBound:max_y+bufferBound,min_x-bufferBound:max_x+bufferBound);
for i = 1 : build_size(b)
XArraySub(b,i) = XArray(b,i) - min_x + 1 + bufferBound;
YArraySub(b,i) = YArray(b,i) - min_y + 1 + bufferBound;
end
min_x_sub = min(XArraySub(b,1:build_size(b)));
max_x_sub = max(XArraySub(b,1:build_size(b)));
min_y_sub = min(YArraySub(b,1:build_size(b)));
max_y_sub = max(YArraySub(b,1:build_size(b)));
tempSub=temp(min_y_sub-bufferBound:max_y_sub+bufferBound,min_x_sub
bufferBound:max_x_sub+bufferBound);
if DISPLAY_MODE == 1
figure(1);
set(1,'Name','Original Image')
imshow(tempSub);
end;
[subH subW] = size(tempSub); % Width : X, Height : Y
subH*subW
c_p = 1; % holds the corner count
for p1 = 1 : build_size(b)-1
for p2 = p1+1 : build_size(b)
if XEdgeIndex(b,p1) ~= XEdgeIndex(b,p2)
if (XArraySub(b,p1) == XArraySub(b,p2)) & (YArraySub(b,p1) == YArraySub(b,p2))
corners(b,c_p,1) = XArraySub(b,p1); % 1 for X
corners(b,c_p,2) = YArraySub(b,p1); % 2 for Y
c_p = c_p + 1; % Fetch a new corner

```

```

end
end
end
end
corner_count(b) = c_p - 1;
for c1 = 1 : corner_count(b)-1
for c2 = c1+1 : corner_count(b)
if corners(b,c1,1) == corners(b,c2,1) % If Xs are matched
if corners(b,c1,2) == corners(b,c2,2) % If Ys are also matched
corners(b,c2,1) = 0; % Remove the X part
corners(b,c2,2) = 0; % Remove the Y part
end
end
end
end
n_c_p = 1; % new corner count
for cnew = 1 : corner_count(b)
if (corners(b,cnew,1) ~= 0) & (corners(b,cnew,2) ~= 0)
new_corners(b,n_c_p,1) = corners(b,cnew,1);
new_corners(b,n_c_p,2) = corners(b,cnew,2);
n_c_p = n_c_p + 1;
end
end
new_corner_count(b) = n_c_p - 1;
corner_edges = zeros(new_corner_count(b),2);
cnt = 1;
for cor = 1 : new_corner_count(b)
for t = 1 : build_size(b)
if (XArraySub(b,t) == new_corners(b,cor,1)) & (YArraySub(b,t) == new_corners(b,cor,2))
corner_edges(cor,cnt) = XEdgeIndex(b,t);
cnt = cnt + 1;
end
end
cnt = 1;
end

```



```

for i = 1 : build_size(b) % i indicates the entry-id(row-id) in each building
s(b,i) = struct('X',a(i,1),'Y',a(i,2),'edgeIndex', a(i,3)); % s is structure that holds each buildings'
end
for i = 1 : build_size(b)
XArray(b,i) = s(b,i).X;
YArray(b,i) = s(b,i).Y;
XEdgeIndex(b,i) = s(b,i).edgeIndex;
end
min_x = min(XArray(b,1:build_size(b)));
max_x = max(XArray(b,1:build_size(b)));
min_y = min(YArray(b,1:build_size(b)));
max_y = max(YArray(b,1:build_size(b)));
temp = im(min_y-bufferBound:max_y+bufferBound,min_x-bufferBound:max_x+bufferBound);
for i = 1 : build_size(b)
XArraySub(b,i) = XArray(b,i) - min_x + 1 + bufferBound;
YArraySub(b,i) = YArray(b,i) - min_y + 1 + bufferBound;
end
min_x_sub = min(XArraySub(b,1:build_size(b)));
max_x_sub = max(XArraySub(b,1:build_size(b)));
min_y_sub = min(YArraySub(b,1:build_size(b)));
max_y_sub = max(YArraySub(b,1:build_size(b)));
tempSub = temp(min_y_sub-bufferBound:max_y_sub+bufferBound,min_x_sub-
bufferBound:max_x_sub+bufferBound);
im1 = tempSub; % A copy of the original building image is stored in 'im'.
[rows, cols] = size(tempSub);
fprintf(fid3, '%d\n', rows*cols);
for i=1 : rows
for j=1 : cols
if tempSub(i,j) < intensity_thr
tempSub(i,j) = 0;
end
end
end
edge_count = 0;
building_area = rows * cols;
for i=1 : rows
for j=1 : cols

```

```

if tempSub(i,j) > 0
edge_count = edge_count + 1;
end
end
end
unit_area_edge_count = edge_count / building_area;
percentage_area_edge_count = unit_area_edge_count * 100;
fprintf(fid2, 'Building Ratio : %f\n', percentage_area_edge_count);
[imDummy orient] = canny2(im1,1); % Sigma = 1
angleCat = zeros(12,1); % 12 Angle Intervals between 0 and 180
for i=1 : rows
for j=1 : cols
if orient(i,j) >= 0 & orient(i,cols) < 15
angleCat(1) = angleCat(1) + 1;
elseif orient(i,j) >= 15 & orient(i,j) < 30
angleCat(2) = angleCat(2) + 1;
elseif orient(i,j) >= 30 & orient(i,j) < 45
angleCat(3) = angleCat(3) + 1;
elseif orient(i,j) >= 45 & orient(i,j) < 60
angleCat(4) = angleCat(4) + 1;
elseif orient(i,j) >= 60 & orient(i,j) < 75
angleCat(5) = angleCat(5) + 1;
elseif orient(i,j) >= 75 & orient(i,j) < 90
angleCat(6) = angleCat(6) + 1;
elseif orient(i,j) >= 90 & orient(i,j) < 105
angleCat(7) = angleCat(7) + 1;
elseif orient(i,j) >= 105 & orient(i,j) < 120
angleCat(8) = angleCat(8) + 1;
elseif orient(i,j) >= 120 & orient(i,j) < 135
angleCat(9) = angleCat(9) + 1;
elseif orient(i,j) >= 135 & orient(i,j) < 150
angleCat(10) = angleCat(10) + 1;
elseif orient(i,j) >= 150 & orient(i,j) < 165
angleCat(11) = angleCat(11) + 1;
elseif orient(i,j) >= 165 & orient(i,j) <= 180
angleCat(12) = angleCat(12) + 1;
end
end
end

```

**APPENDIX G: THE DISTRIBUTION OF THE COLLAPSED, UN-COLLAPSED AND INCORRECTLY DETECTED BUILDINGS FOR THE WATERSHED SEGMENTATION APPROACH**

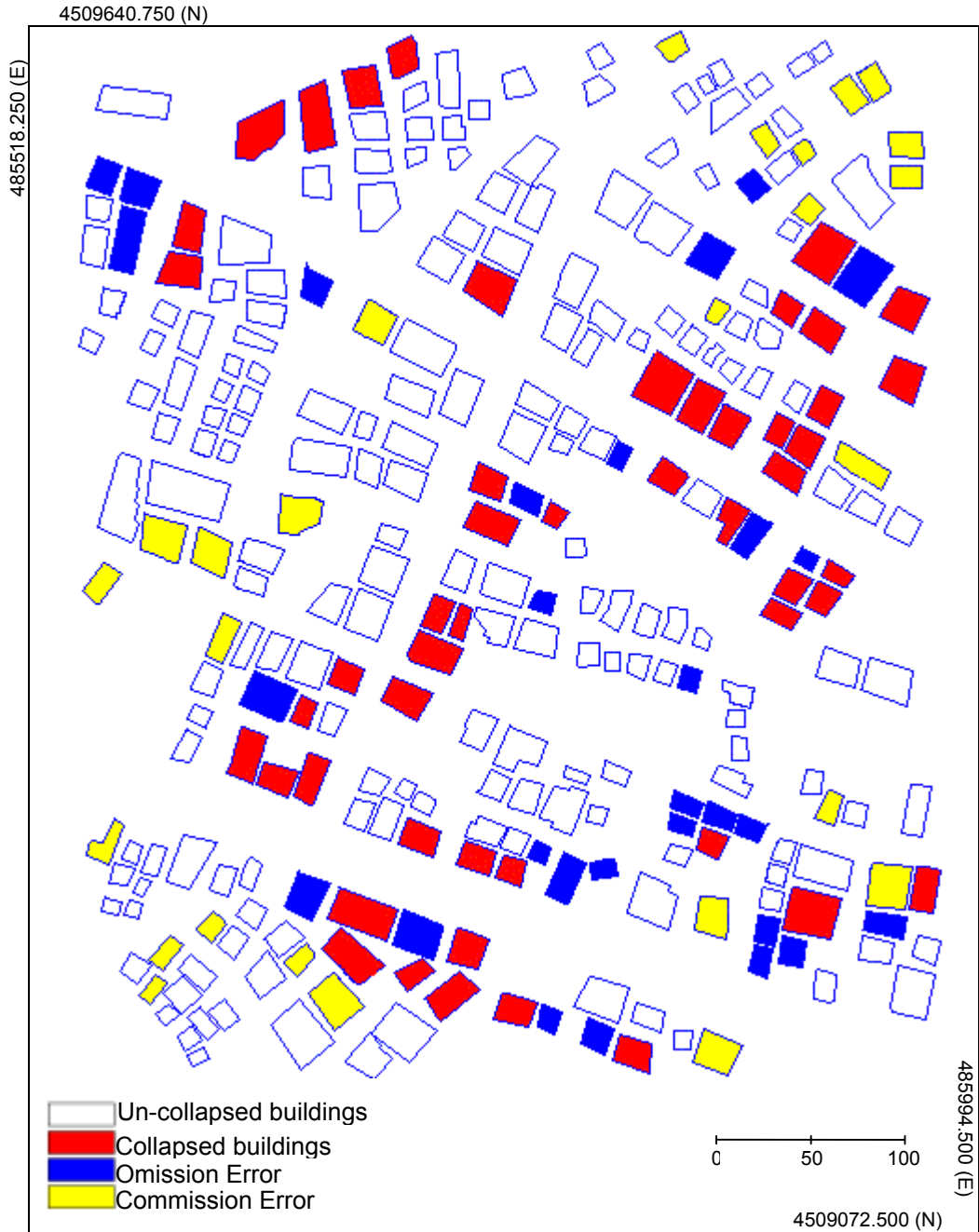


Figure G.1. The building distribution for the Watershed Segmentation Approach

**APPENDIX H: THE DISTRIBUTION OF THE COLLAPSED, UN-COLLAPSED  
AND INCORRECTLY DETECTED BUILDINGS FOR THE  
BUILDING INTENSITY - GRADIENT ORIENTATION  
APPROACH**

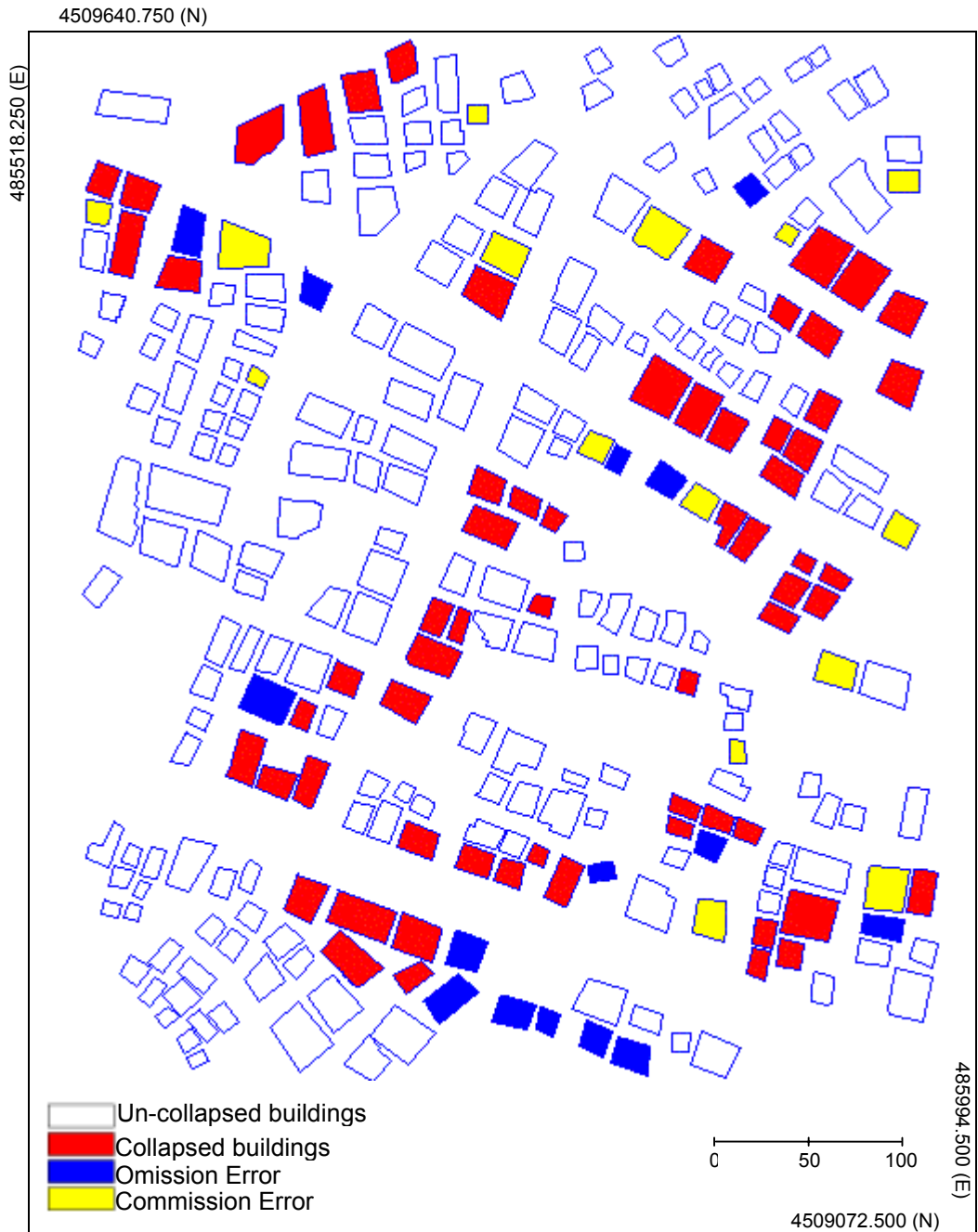


Figure H.1. The building distribution for the Building Intensity - Gradient Orientation Approach

**APPENDIX I: THE DISTRIBUTION OF THE COLLAPSED, UN-COLLAPSED AND INCORRECTLY DETECTED BUILDINGS FOR THE BUILDING INTENSITY - GRADIENT ORIENTATION APPROACH WITH A ONE-PIXEL WIDE BUFFER**

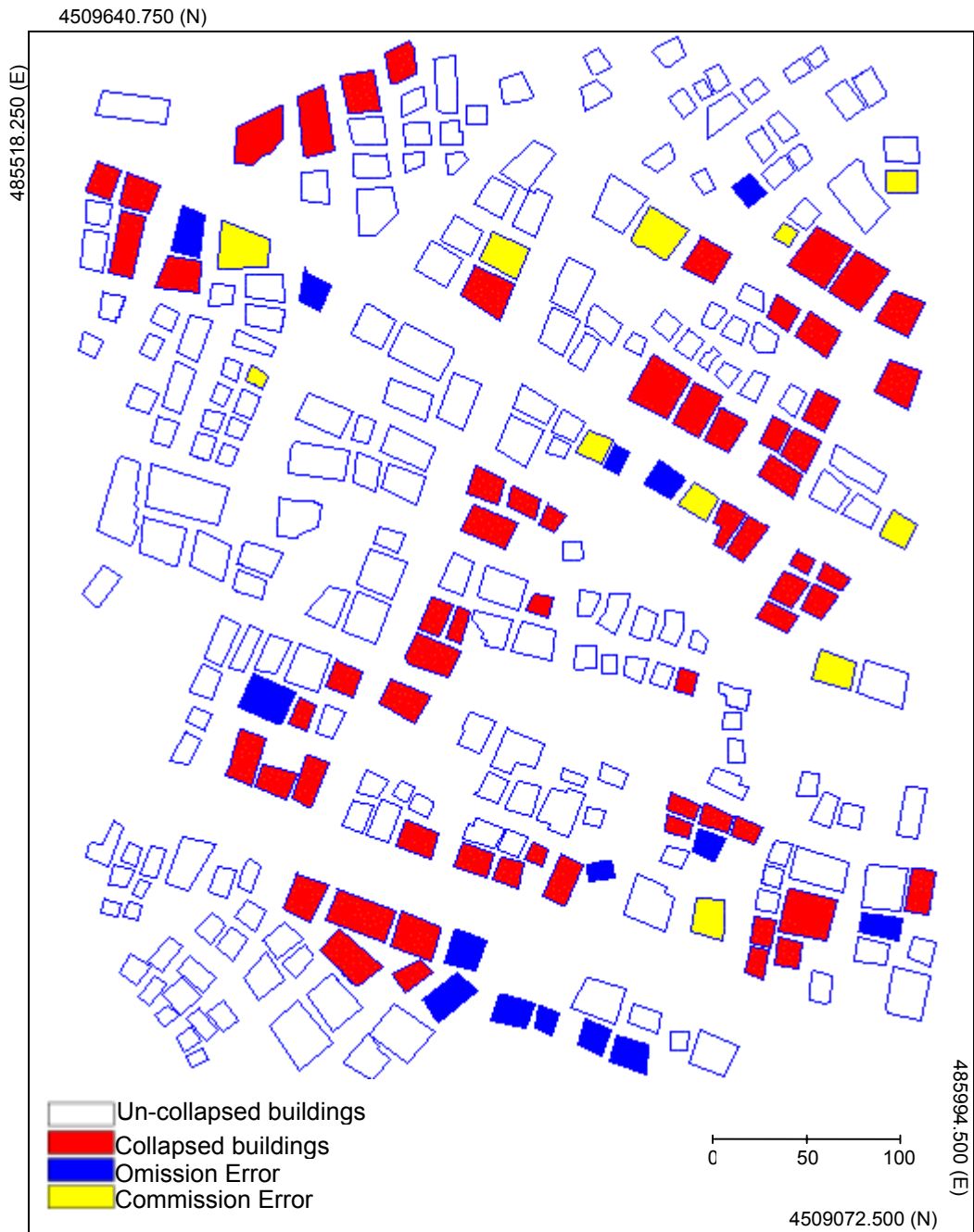


Figure I.1. The building distribution for the Building Intensity - Gradient Orientation Approach with a one-pixel wide buffer